Theory of the spin excitations of $Rb_2Mn_xNi_{1-x}F_4$

S. Kirkpatrick
IBM Thomas J. Watson Research Center, Yorktown Heights, New York 10598

A. B. Harris *
Department of Physics, University of Pennsylvania, Philadelphia, Pennsylvania 19174

(Received 1 April 1975)

We give a systematic treatment of the spin excitations of a family of disordered quasi-two-dimensional Heisenberg antiferromagnets, $Rb_2Mn_xNi_{1-x}F_4$, for arbitrary values of x. The density of states, static response functions, and the dynamic susceptibility are calculated numerically. Results at several concentrations are presented graphically. We derive simple analytic theories which give an adequate description of the calculated quantities. The static response functions characterize excitations at low energy and long wave length, and enable us to predict the concentration dependence of the anisotropy gap frequency and the temperature dependence of the magnetization. The dynamic susceptibility is in good agreement with recent neutron-scattering experiments on $Rb_2Mn_{0.5}Ni_{0.5}F_4$. The spin-wave density of states for $0.1 < x < 1$ is found to split into two separated subbands, consisting essentially of Mn and Ni spin excitations, respectively. The evolution of the two subbands as a function of concentration is studied through the dynamic susceptibility, which resolves both q and ω, and by numerical tests for localization of the normal modes. The two-mode character of this system persists even after the gap between subbands has closed to become a pseudogap.

I. INTRODUCTION

Transition-metal fluorides of the form TF_2, ATF_3, and A_2TF_4, where A represents an alkali metal, usually K or Rb, and T an iron-group transition metal, are a family of insulating antiferromagnets about which a great deal is known. Their magnetic properties are accurately described by the Heisenberg Hamiltonian

$$\mathcal{H} = 2\sum_{i<j} J_{ij}\vec{S}_i\cdot\vec{S}_j - \sum_i (\sigma_i \Delta_i S_i^z + g_i \mu_B \vec{h}_i^{\,\mathrm{ext}}(t)\cdot\vec{S}_i)\,, \tag{1}$$

in which J_{ij} is the positive exchange interaction between neighboring spins $\vec{S}_i$ and $\vec{S}_j$ on sites i and j, Δ_i is a uniaxial anisotropy energy, g_i is the g factor for atom i, h^{ext} is an external field, μ_B is the Bohr magneton, and

$$\sigma_i = \begin{cases} 1 & \text{on even sublattice sites}\,, \\ -1 & \text{on odd sublattice sites.} \end{cases} \tag{2}$$

Nearest-neighbor exchange has been found to dominate Eq. (1) in these compounds. These materials and their alloys have recently been reviewed by de Jongh and Miedema[1] and by Cowley and Buyers.[2]

In this paper we shall give a systematic theoretical study of the family $Rb_2Mn_xNi_{1-x}F_4$, an alloy system which is just beginning to attract experimental interest.[3] In the tetrafluorides, the transition-metal ions form layers separated sufficiently to be treated as independent two-dimensional (2D) square lattices. Since Rb_2MnF_4 and Rb_2NiF_4 differ considerably in the strength of their magnetic interactions (the ordering temperatures[4] are 38.4 and 91 K, respectively), we can expect the effects of disorder to be prominent in the alloy system.

All the parameters to be used in the Hamiltonian (1) for $Rb_2Mn_xNi_{1-x}F_4$ are known to roughly 10% accuracy, either from measurements on the pure 2D systems,[1] or from measurements at low concentrations on mixed 3D systems.[2] Cowley and Buyers find that the expression for the exchange interaction between different components, A and B,

$$J_{AB} = (J_{AA}J_{BB})^{1/2}\,, \tag{3}$$

which would be expected from superexchange theory, is in error by only ±5% for most iron-group metal ions as impurities in manganese fluorides. From Raman-scattering studies of the local impurity mode of low concentrations of Ni in the perovskite $KMnF_3$, Thorpe[5] has extracted a value of J_{MnNi} about 1% greater than would be given by Eq. (3).

In Rb_2NiF_4, the anisotropy terms in Eq. (1) originate from local crystal-field splittings. Therefore, Δ_i on Ni sites should have essentially the same value in the alloy as in the pure system. In Rb_2MnF_4, however, the anisotropy is much smaller and of dipolar origin.[6] Thus Δ_i on Mn sites is proportional to the average magnetic moment per site in the alloy. This dependence of Δ_i on composition has only a small effect on the properties considered here, and will therefore be neglected. $Rb_2Mn_xNi_{1-x}F_4$ is thus to a good approximation a strongly disordered material for which a microscopic model exists with no unknown parameters. It can furnish a critical test of theory and of

our intuitions about excitations in disordered systems.

In principle, there are at least three distinct regions of concentration which must be considered. It is known from studies of 2D site percolation[7,8] that for $x<0.4$ all of the Mn atoms will lie in isolated finite clusters, surrounded by Ni atoms, a large fraction of which will be part of an infinite connected cluster which spans the crystal. Likewise, for $x>0.6$, the Ni atoms will be isolated in clusters in a Mn host. At the intermediate concentrations, only finite clusters are found. Spin excitations which extend over large distances should have different characteristics in the three regions. We shall also find below that the region of low Mn concentration introduces some novel features.

Isolated clusters are not necessarily small, especially in the intermediate-concentration regime. Dean and Bird[9] have studied the cluster statistics of the randomly diluted 2D square lattice with nearest-neighbor interactions, and find that at 50% occupation of the sites, the largest clusters in their Monte Carlo samples of 62 500 sites contained more than 300 connected atoms. For this case, the average cluster contained roughly 8 atoms. Although the average cluster size decreases rapidly at lower concentrations, some large clusters will still occur. Dean and Bird found an average connected cluster size of 3 sites at 35% occupation, but each of their samples contained a few clusters of 40 or more sites. Above the percolation threshold, isolated small clusters separated from the infinite cluster persist, their average size decreasing with increasing x. For 67.5% occupation, the average isolated cluster size was found to be 1.9 sites, with a few clusters of 15–30 sites always present. It appeared in this numerical study that for the same mean isolated cluster size, larger fluctuations in the size of the rare large isolated clusters observed occur above the percolation threshold than below it. Study of the strongly disordered $Rb_2Mn_xNi_{1-x}F_4$ system thus should afford the opportunity to analyze the effects of both large and small localized states, as well as the feature, unique to 2D, of an intermediate region in which only isolated clusters are present. There are other advantages to studying effects of disorder in 2D rather than 3D systems. Not only are the effects, in general, larger, but numerical calculations such as we shall describe are more practical.

Several strongly disordered 3D insulating antiferromagnets have been studied previously by neutron scattering,[10] but the only experimental studies of spin excitations in 2D mixed systems of which we are aware are on $Rb_2Mn_{0.5}Ni_{0.5}F_4$, by Birgeneau *et al.*[3] Using inelastic neutron scattering, they have observed two sets of excitations: a branch consisting of sharp lines extending between 1 and 9 meV, and a second set of broad lines at energies above 16 meV. Since the energies of the centers of both lines shift with momentum transfer q, both were characterized as propagating excitations. A four-sublattice model for the system was proposed in Ref. 3 to interpret the two modes. Ni and Mn atoms on each sublattice are distinguished, and assumed to satisfy the averaged equations of motion. This model predicts two modes of zero width for each value of q, and gives wave functions which can be used to calculate scattering intensities. On the basis of these wave functions, Birgeneau *et al.*[3] interpret the second band as a propagating "optical" mode, in which the Ni and Mn spins of each sublattice move in opposite directions. Some of the 3D systems studied by Svensson *et al.*[10] also display this sort of two-mode behavior.

Alben and Thorpe[11] have recently performed a Monte Carlo calculation of the neutron-scattering intensities for $x=0.5$, using Eq. (1) as the Hamiltonian, and making the assumption (3). Their results are in good agreement with those of Birgeneau *et al.*, and furnish support for our conjecture that Eqs. (1) and (3) should apply to the $Rb_2Mn_xNi_{1-x}F_4$ system at arbitrary x.

The density of states for the closely related $K_2Mn_{0.5}Ni_{0.5}F_4$ has been evaluated numerically by Huber.[12] Although his results, based on a small (30×30) sample with free edge boundary conditions, are crude, Huber also observed two subbands, separated in energy by a gap. Reasoning by analogy with examples of strong scattering which have been studied elsewhere in the disordered electron and phonon problem,[13,14] he identified the lower band as due to excitations involving Mn spins, and the upper band as due to Ni.

Our studies show that this two-band behavior is not restricted to $x=0.5$, but occurs at all but the lowest Mn concentrations. We support Huber's interpretation of the character of the two subbands, as opposed to the "optical-mode" picture, and present calculations below which quantify the amount of participation by Ni spins in the lower subband, and vice versa, as well as the regions of q space in which it occurs. By measuring the sensitivity of specific eigenvalues of our Monte Carlo samples to changes in the boundary conditions, it is possible to determine the localized or extended character of a state directly. In this way we find that all of the states in the Ni subband at $x=0.5$ are localized, despite the fact that the energy at which their scattering is strongest shifts with wave vector. By combining the Monte Carlo studies at arbitrary concentrations with exact treatments of the effects of very low concentrations of Mn in Rb_2NiF_4 or vice versa, we can assemble a comprehensive picture of the phenomena associated

with the formation of the two subbands in the alloy. Finally, we have carried out numerical calculations of the dynamical susceptibility which are in agreement with the scattering experiments, and can be used to give a more detailed characterization of the eigenmodes than is possible from consideration of the density of states alone.

The paper is organized as follows. In Sec. II we give derivations of most of the physical quantities which can be obtained either by exact solution of the case of a single impurity[15–17] or from a microscopic Monte Carlo model of the random magnetic system. We present calculations of the densities of states of four samples, representing the different concentration regimes of interest. In two of these cases, we have tested for the presence or absence of extended states.

In Sec. III the extended states at low energy are studied by first expressing their energies in terms of static response functions, then calculating those response functions numerically for Monte Carlo samples. A report on the application of this type of analysis to ferromagnets, ferrimagnets, and antiferromagnets is in preparation. A summary of those results has appeared elsewhere.[18] In the present work we consider only antiferromagnets, and treat explicitly the presence of atoms with differing g values. Calculations of the anisotropy, exchange stiffness, and various susceptibilities as functions of concentration are presented, and used to predict the gap frequency and the temperature dependence of the magnetization. These predictions of dynamics from static properties are in agreement with the small amount of experimental data that exists, as well as with dynamical calculations on the Monte Carlo samples. They can readily be tested by future experiments.

Calculations of the dynamic susceptibility $\chi''(q, \omega)$ are presented in Sec. IV for four concentrations, and compared at $x = 0.5$ with the neutron-scattering experiments, which measure the same quantity. The systematic trends in the types of states which are found as x, q, and ω are varied and discussed. We compare several theories for the mode frequencies. A relatively simple estimate based on moments of the average susceptibility is found to give accurate predictions of the positions of the high-energy peaks. This method introduces no assumptions of homogeneity or that states are all either extended or localized. Partial susceptibilities, which separate the contributions of the two types of atoms to $\chi''(q, \omega)$ are also discussed in Sec. IV. They are useful in testing the validity of approximate pictures, including the four-sublattice model, of the character of the modes of this system.

Some details of the numerical techniques we employed are given in Appendix A. Appendix B contains the details of our calculations of various response functions for the case of a single impurity atom. In Appendix C, the formulas needed to evaluate moments of $\chi''(q, \omega)$ are tabulated. In Appendix D, we derive the dynamic susceptibility for the four-sublattice model.

II. DENSITY OF STATES

The equations of motion for a spin deviation

$$\delta\vec{S}_i(t) = S_i^+(\omega)(\hat{x} + i\hat{y})e^{-i\omega t} , \tag{4}$$

where $\hat{x}$ and $\hat{y}$ are unit vectors, obtained from the Hamiltonian (1) in the presence of an external field

$$\vec{h}_i(t) = h_i(\omega)(\hat{x} + i\hat{y})e^{-i\omega t} , \tag{5}$$

are

$$\hbar\omega S_i^+(\omega) = 2\sum_j J_{ij}(S_i^z S_j^+ - S_j^z S_i^+) + \sigma_i \Delta_i S_i^+ - 2g_i \mu_B h_i(t) S_i^z , \tag{6}$$

where μ_B is the Bohr magneton. If we linearize about the Néel state, in which

$$\langle S_i^z \rangle = \sigma_i S_i , \tag{7}$$

where S_i is the magnitude of the spin on site i, the equations of motion become

$$\hbar\omega S_i^+(\omega) = 2\sum_j \sigma_i J_{ij}[S_i S_j^+(\omega) + S_j S_i^+(\omega)] + \sigma_i[\Delta_i S_i^+(\omega) - 2g_i \mu_B h_i(\omega) S_i] . \tag{8}$$

Equations (8) may be transformed into

$$\sum_j M_{ij}(\omega) S_j^+(\omega) = -2g_i \mu_B h_i(\omega) S_i , \tag{9}$$

where

$$M_{ij} = \delta_{ij}\left(\sigma_i \hbar\omega - \Delta_i - 2\sum_k J_{ik} S_k\right) - 2J_{ij} S_i . \tag{10}$$

The matrix $\underline{M}$ is not symmetric, which complicates both numerical work and discussion of its eigenstates. We can remedy this by introducing

$$S_i^+(\omega) = S_i^{-1/2} S_i^+(\omega) . \tag{11}$$

These satisfy symmetric equations

$$\sum_j N_{ij} s_j^+(\omega) = -2g_i \mu_B h_i(\omega) S_i^{1/2} , \tag{12}$$

where

$$N_{ij} = \delta_{ij}\left(\sigma_i \hbar\omega - \Delta_i - 2\sum_k J_{ik} S_k\right) - 2J_{ij}(S_i S_j)^{1/2} . \tag{13}$$

It is convenient to define a dynamical matrix $\underline{W}$ by writing $\underline{N}$ in the form

$$\underline{N} = \underline{\sigma}\hbar\omega - \underline{W} , \tag{14}$$

where $\underline{\sigma}$ is a diagonal matrix with elements σ_i.

Since the eigenvalues of the original system (8) are the same as those of (13), and the eigenvectors are related by the transformation (11), we can discuss one-magnon excitations by examining the eigenstates of (13).

For comparison with experiment, we also need various susceptibilities. The most general two-point susceptibility is defined by

$$\chi_{ij}(\omega) = g_i \mu_B S_i^+(\omega)/h_j(\omega) \tag{15}$$

$$= -2 g_i \mu_B S_i^{1/2} (\underline{N}^{-1})_{ij} g_j \mu_B S_j^{1/2} \, . \tag{16}$$

Its Fourier transform

$$\chi(\vec{q}, \omega) = \frac{1}{V} \sum_{ij} \exp[i\vec{q} \cdot (\vec{R}_j - \vec{R}_i)] \chi_{ij}(\omega) \, , \tag{17}$$

where V is the volume of the crystal, can be expressed in the symmetric form

$$\chi(\vec{q}, \omega) = -2 \langle \vec{q} | \underline{N}^{-1}(\omega) | \vec{q} \rangle \, , \tag{18}$$

where

$$\langle i | \vec{q} \rangle = g_i \mu_B (S_i/V)^{1/2} \exp(i\vec{q} \cdot \vec{R}_i) \, . \tag{19}$$

In order to study the nature of the elementary excitations it is useful to distinguish the role of the two different types of atoms by defining partial susceptibilities. To do this, we define a diagonal projection operator P_α which is unity for sites occupied by atoms of the type α and zero otherwise. Then we write

$$\chi_{\alpha\beta} = -2 \langle \vec{q} | P_\alpha \underline{N}^{-1}(\omega) P_\beta | \vec{q} \rangle \, . \tag{20}$$

We shall now consider excitations of the spin system in the absence of external fields. $\underline{N}$ has both positive and negative eigenfrequencies, but on the average the spectrum is symmetric about zero, so we shall only consider the positive frequencies. Formally, the density of states can be extracted from $\underline{N}$ by

$$\rho(\omega) = \frac{1}{N\pi} \lim_{\epsilon \to 0^+} \operatorname{Im} \operatorname{Tr} \underline{\sigma} \underline{N}^{-1}(\omega - i\epsilon) \, , \tag{21}$$

where Tr denotes the trace and N is the total number of sites. Even frequency moments of $\rho(\omega)$ are easily calculated (odd moments vanish on the average by symmetry) by expanding $\underline{N}^{-1}$ for large ω:

$$\underline{\sigma} \underline{N}^{-1}(\omega) = (\hbar\omega - \underline{\sigma} \underline{W})^{-1}$$

$$= \sum_n (\hbar\omega)^{-n-1} (\underline{\sigma} \underline{W})^n \, . \tag{22}$$

An integral over the density of states as given by Eq. (21) with ω^{2m} in the integrand can be transformed into a contour integral which picks out the coefficient of ω^{-2m-1} in Eq. (22). (See Ref. 13, Sec. 3, for a fuller discussion of the derivation of moments.) The configurational averages of the quantities in Eq. (22), denoted $(\ )_{av}$, can be carried out explicitly. For example,

$$(\hbar\omega)^2_{av} = (1/N)(\operatorname{Tr} \underline{\sigma} \underline{W} \underline{\sigma} \underline{W})_{av} \tag{23}$$

$$= \left[\left(\sum_k J_{ik} S_k + \Delta_i \right)^2 - \sum_k J_{ik} J_{ki} S_i S_k \right]_{av} \tag{24}$$

was used to check the accuracy of the calculated densities of states reported in this section. More interesting are the projected moments,

$$(\hbar\omega_\alpha)^2_{av} = (1/N_\alpha)(\operatorname{Tr} P_\alpha \underline{\sigma} \underline{W} \underline{\sigma} \underline{W})_{av} \tag{25a}$$

$$= \left(\Delta_\alpha + z \sum_\beta x_\beta J_{\alpha\beta} S_\beta \right)^2 - \sum_\beta z x_\beta J_{\alpha\beta}^2 S_\alpha S_\beta \, , \tag{25b}$$

where α or β can stand for either Mn or Ni, S_α is the spin of an α atom, N_α is the number of α atoms, and so forth. Thus Eq. (25) gives moments over the density of states weighted by the amplitude of the average spin deviation of the states on the atoms in question.

In the numerical calculations which follow, we shall adopt the parameters cited by Birgeneau *et al.*,[3] although our definition of J differs from theirs by a factor of 2. These are $J_{MnMn} = 0.328$ meV,

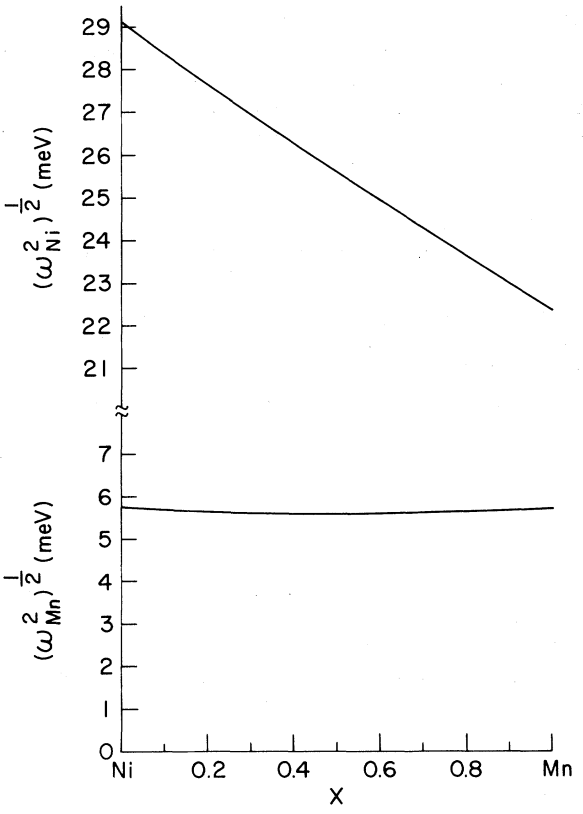

FIG. 1. Characteristic frequencies $(\omega^2_{Ni})^{1/2}_{av}$ and $(\omega^2_{Mn})^{1/2}_{av}$ for Ni and Mn excitations, respectively, as functions of Mn concentration x. The characteristic frequencies are defined in terms of moments of the density of states in Eq. (25).

$J_{MnNi} = J_{NiMn} = 1.17$ meV, $J_{NiNi} = 4.15$ meV, $\Delta_{Mn} = 0.03$ meV, and $\Delta_{Ni} = 0.28$ meV. The remaining parameters needed to specify the alloy system are $g_{Mn} = 2.0$, $g_{Ni} = 2.22$,[19] $S_{Mn} = 2.5$, and $S_{Ni} = 1.0$.

Because of the marked difference between the rms characteristic frequencies derived from the projected second moments, as plotted in Fig. 1, we can expect to find striking differences in the dynamics of Ni and Mn spins in the mixed systems. The characteristic frequency of the excitations seen at a Mn site $(\hbar\omega^2_{Mn})^{1/2}_{av}$ is nearly concentration independent and equal to about 5.5 meV. The frequency characterizing the Ni excitations decreases with decreasing Ni concentration, but is never less than 22 meV, a value greater than the highest single magnon energies (6.6 meV) expected for pure Rb_2MnF_4. Thus Ni spins at low concentration will give rise to an isolated high-frequency localized level, and we must expect to find a two-band density of states at intermediate concentrations. That is, there will be two distinct parts to $\rho(E)$, one consisting of excitations involving mostly Ni spins and one mostly Mn. Since the characteristic frequency for Mn spins exceeds the gap frequency (4.3 meV) for Rb_2NiF_4 magnons, there will be a strong effect caused by Mn impurities in the bottom of the Ni magnon band. However, a more detailed analysis is needed to tell whether localized impurity modes will occur in the Ni gap at low Mn concentrations.

The low-concentration regimes, when small numbers of Mn spins are substituted into the Ni compound and vice versa, can be treated essentially exactly. The solution of the single-defect problem has already been studied extensively,[15-17] so we will not discuss the formalism in detail, but will concentrate mainly on a presentation of numerical results.

We will study the spin Green's function $G_{ij}(\omega)$ defined by

$$G_{ij}(\omega) = \int G_{ij}(t) e^{i\omega t}\, dt \,, \tag{26}$$

$$G_{ij}(t) = [\Theta(t)/i\hbar]\langle [S_i^+(t),\ S_j^-(0)]\rangle \,, \tag{27}$$

where $\langle\ \rangle$ indicates a thermal average, which in this case we take as a ground-state average, and $\Theta(t) = 1$ for $t > 0$ and zero for $t < 0$. Neglecting spin-wave interactions and deviations from the Néel ground state we may write the equations of motion for the spin Green's function as

$$\sum_j M_{ij}(\omega)\, G_{jk}(\omega) = \delta_{ik} 2S_i \,, \tag{28a}$$

where $\underline{M}$ was defined in (10). We shall define $G_{jk} = 2\sigma_j H_{jk}$, in terms of which Eq. (28a) becomes

$$\sum_j L_{ij} H_{jk} = \delta_{ik} \,, \tag{28b}$$

where $L_{ij} = S_i^{-1} M_{ij} \sigma_j S_j$. In the case of a single defect at the lattice site m one writes

$$L_{ij}(\omega) = L^0_{ij} + V^m_{ij} \,, \tag{29}$$

where L^0_{ij} is the value of L_{ij} for the pure crystal. One can then write the solution for $\underline{H}$

$$\underline{H} = \underline{H}^0 + \underline{H}^0\, \underline{t}^m\, \underline{H}^0 \,, \tag{30}$$

where $\underline{t}^m$ is the t matrix associated with $\underline{V}^m$:

$$\underline{t}^m = \underline{V}^m (\underline{I} - \underline{H}^0 \underline{V}^m)^{-1} \,. \tag{31}$$

In discussing the t matrix it is convenient to introduce the following symmetry adapted basis functions[20]:

$$\begin{aligned}
&|\varphi_{s1}\rangle = |m\rangle \,, \quad |\varphi_{s2}\rangle = \sum_{\vec{\delta}} \tfrac{1}{2} |m + \vec{\delta}\rangle \,, \\
&|\varphi_{px}\rangle = (|m + a\hat{x}\rangle - |m - a\hat{x}\rangle)/2^{1/2} \,, \\
&|\varphi_{py}\rangle = (|m + a\hat{y}\rangle - |m - a\hat{y}\rangle)/2^{1/2} \,, \\
&|\varphi_{d}\rangle = (|m + a\hat{x}\rangle + |m - a\hat{x}\rangle - |m + a\hat{y}\rangle - |m - a\hat{y}\rangle)/2 \,,
\end{aligned} \tag{32}$$

($\vec{\delta}$ denotes one of the nearest-neighbor positions $\pm a\hat{x}$ or $\pm a\hat{y}$) in terms of which

$$\begin{aligned}
t^m = t^{(s)} &+ |\varphi_{px}\rangle t_p \langle \varphi_{px}| \\
&+ |\varphi_{py}\rangle t_p \langle \varphi_{py}| + |\varphi_d\rangle t_d \langle \varphi_d| \,,
\end{aligned} \tag{33}$$

where

$$t^{(s)} = \sum_{ij} t^{(s)}_{ij} |\varphi_{si}\rangle \langle \varphi_{sj}| \,. \tag{34}$$

We express the density of states in terms of t^m by

$$\begin{aligned}
N\pi\rho(\omega) &= \mathrm{Tr}\, \mathrm{Im}\, \underline{L}^{-1}(\omega - i\epsilon) \\
&= \mathrm{Im} \sum_i H_{ii}(\omega - i\epsilon) \,,
\end{aligned} \tag{35}$$

and if we write $\rho(\omega) = \rho^0(\omega) + N^{-1}\delta\rho(\omega)$, where $\rho^0(\omega)$ is the density of states of the pure crystal, we have

$$\delta\rho(\omega) = \pi^{-1}\, \mathrm{Im} \sum_{ijk} H^0_{ij}(\omega - i\epsilon) t^m_{jk}(\omega - i\epsilon) H^0_{ki}(\omega - i\epsilon) \,. \tag{36}$$

It can be shown that

$$\hbar \sum_i H^0_{ij} H^0_{ki} = -\frac{dH^0_{ki}}{d\omega} \,, \tag{37}$$

so that

$$\hbar\delta\rho(\omega) = -\pi^{-1} \frac{d}{d\omega} \left(\mathrm{Im} \sum_{ij} H^0_{ij}(\omega - i\epsilon) t^m_{ji}(\omega - i\epsilon) \right) \tag{38a}$$

$$= \pi^{-1} \frac{d}{d\omega} \left(\mathrm{Im}\, \mathrm{Tr} \ln(\underline{I} - \underline{H}^0 \underline{V}^m) \right) \,, \tag{38b}$$

which is the usual phase-shift formula.[21] That is, we set $\det(\underline{I} - \underline{H}^0 \underline{V}^m) = e^{i\delta(\omega)}$ and we obtain

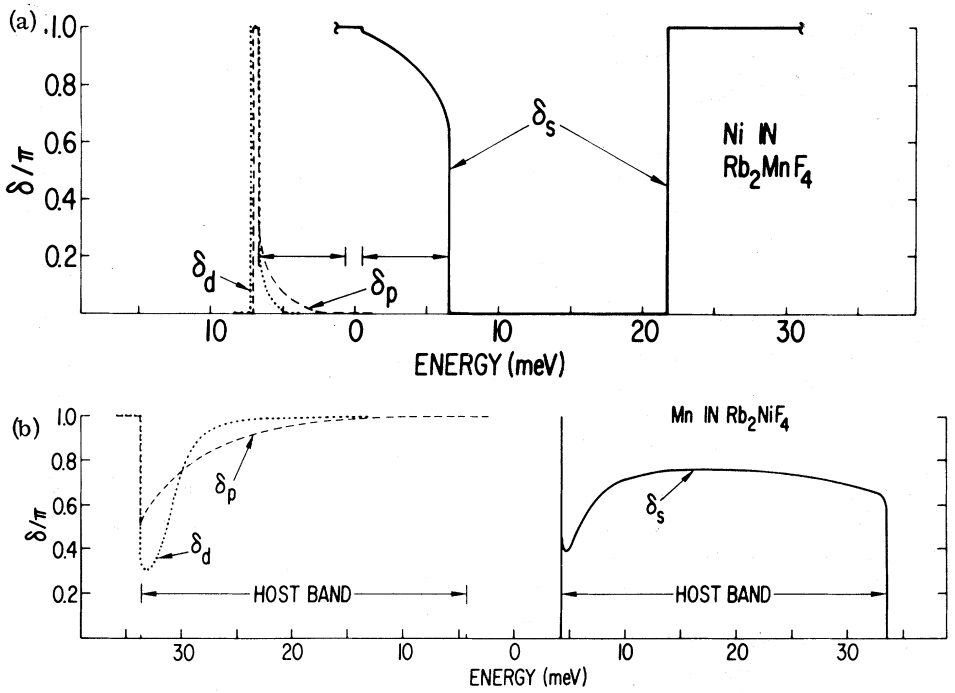

FIG. 2. Phase shifts for s-wave (solid line), p-wave (dashed line), and d-wave (dotted line) scattering by a single impurity atom. (a) The case of a Ni atom added to Rb_2MnF_4; (b) describes Mn in Rb_2NiF_4. Change in the density of states associated with each partial wave can be obtained from the slopes of the individual phase shifts by (39). Horizontal arrows in each figure indicate the extent of the host magnon band.

$$\hbar\delta\rho(\omega) = \pi^{-1}\frac{d[\delta(\omega)]}{d\omega} \quad . \tag{39}$$

In Figs. 2(a) and 2(b) we show the results for $\delta_\alpha(\omega)$, where α is the symmetry label, s, p, or d, and

$$\delta(\omega) = \delta_s(\omega) + 2\delta_p(\omega) + \delta_d(\omega) \quad . \tag{40}$$

Figures 2(a) and 2(b) show $\delta_s(\omega)$ for positive frequencies and $\delta_p(\omega)$ and $\delta_d(\omega)$ for negative frequencies. As Kanamori and Tonegawa[15] have explained, $\delta_s(\omega)$ for positive frequencies and $\delta_p(\omega)$ and $\delta_d(\omega)$ for negative frequencies contain information concerning the nonresonant response in which a sublatice is driven opposite to its natural sense of precession. If one follows the variation of $\delta(\omega)$ as ω increases, then the change in the density of states due to the defect is given by Eq. (39).

Consider the case of a Ni defect in the Mn system. Since $J_{MnNi} > J_{MnMn}$, it is clear that a localized Ni state will be formed at $\omega \sim 2zJ_{MnNi}S_{Mn} \sim 22$ meV. Thus one s-like state must be removed from the Mn band. From Fig. 2(a) we see that about 0.7 of a state is taken from the extreme high-energy edge of the Mn band at 6.5 meV and the rest is taken more or less uniformly from the entire band. Since $J_{MnNi}S_{Ni} > J_{MnMn}S_{Mn}$, it is possible to form localized modes on the shell of Mn atoms adjacent to the impurity. The p-wave shell mode occurs at $\omega \sim 6.9$ meV and the d-wave mode occurs at $\omega \sim 7.2$ meV. The d-wave states have higher energy than the p-wave states since the former, having larger angular momentum, have more nodes in their wave functions. Again, the states removed from the Mn band come primarily from the energy range above 5 meV. As the Ni concentration is increased we expect the sharp peak at the top of the Mn band to become further eroded. Also, since the binding energy of the shell modes is much less than the width of the pure Mn band, we expect these states to become broad resonances. This picture is easily extended to higher concentrations and is confirmed by the appearance of the Mn band in the numerical work at $x = 0.5$ reported below.

Adding a Mn defect to the pure Ni system [Fig. 2(b)] is more complex. There are no p- or d-wave bound states because the shell modes would have energies within the pure Ni band. About one-half a p-wave and one-half a d-wave state are removed from the top of the host band and are spread to lower energies. There is an s-wave bound state with extremely small (0.033 meV) binding energy E_s. In Fig. 2(b), one sees that one-half of this state comes from the upper band edge, and one-half from the lower band edge. If we relate the

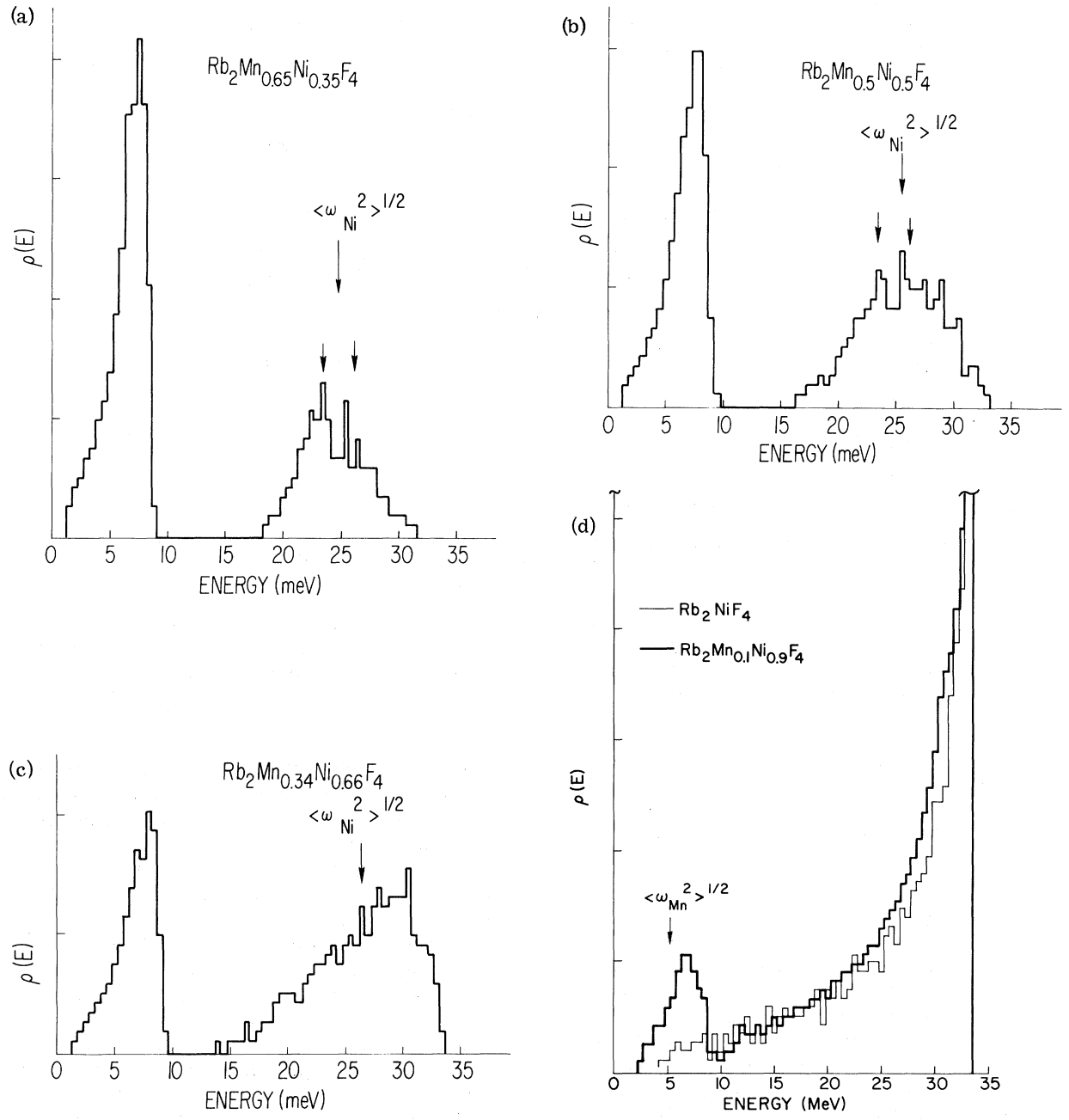

FIG. 3. Single magnon density of states for Mn concentrations $x=0.65$ (a), $x=0.50$ (b), $x=0.34$ (c), and $x=0.10$ (d). Light line in (d) indicates the density of states for Rb_2NiF_4. Vertical scales are the same for Figs. 3(a)–3(c). In Fig. 3(d) one vertical division represents half as many states in Figs. 3(a)–3(c). Arrows in (a) and (b) mark the positions of the lowest two modes predicted by the Ising cluster model (42). The characteristic frequencies for Ni and Mn excitations, defined in (25), are also shown where appropriate.

energies near the host gap frequency ω_0 to q by [see Ref. 22, Eq. (4.10)]

$$\hbar\omega_0 - E_s = \hbar[\omega_0^2 + \omega_E^2(qa)^2/2]^{1/2}\,, \tag{41}$$

where for a pure system $\omega_E = 2JzS$, we obtain $iqa \sim 0.023$, which implies that the bound state size is of the order of 280 lattice constants. It is obvious that the low-concentration regime in this case may be minute. In calculating response functions which describe pulling the Mn spin out of alignment with its neighbors, low-concentration theory may break down when the bound states overlap.

For a response in which Mn and Ni spins move in phase, low-concentration theory may be used to much higher concentration. Low-concentration calculations of the susceptibility χ and the exchange stiffness A are summarized in Appendix B; the results are used in subsequent sections of this paper. From the arguments given above, we conclude that these results for χ will have a smaller range of validity than do those for A.

Now we turn to our numerical results, which are useful at arbitrary concentrations. Densities of states were obtained for four large Monte Carlo samples, each 64-by-64 sites with periodic boundary conditions, representing the four concentration regimes of interest. The results are plotted in Fig. 3 as histograms, sampled at 0.5-meV intervals. The numerical techniques used to obtain Fig. 3 are described in Appendix A. The four regimes and the concentrations chosen to represent them are isolated Ni clusters in a connected Mn host [$x=0.65$, Fig. 3(a)]; both Ni and Mn confined to isolated clusters, which may be rather large [$x=0.5$, Fig. 3(b)]; Ni concentration sufficient to insure connectedness, while the Mn are isolated [$x=0.34$, Fig. 3(c)]; and low Mn concentration [$x=0.1$, Fig. 3(d)]. The low Ni concentration limit will not be considered further in this section, as it is similar to the cases discussed extensively in Refs. 15–17.

In the first three cases, there are two subbands, separated by an apparent gap. This gap cannot be a true gap, with zero density of states. One can argue, following Lifshitz,[22] that there is a finite probability of finding a region sufficiently large and Ni rich to give rise to Ni modes of any energy down to the gap energy, 4.3 meV, of Rb_2NiF_4. Such states deep in a pseudogap are too rare to be seen in a finite sample simulation such as this. However, this argument also suggests that the states that are found at the bottom of the upper subband will form some kind of band tail, and may be localized. There will be a similar tail of rare Mn states down to 0.63 meV, the gap energy of Rb_2MnF_4, but we were not able to observe these in our numerical studies.

The characteristic excitation frequency for Ni spins, $(\omega^2_{Ni})^{1/2}_{av}$, was found to lie in the peak of the upper subband, and is indicated by an arrow in each plot. We carried out a detailed comparison of $(\omega^2_{Ni})_{av}$, and $(\omega^2_{Mn})_{av}$ with the second moments of the upper and the lower subbands, respectively. The characteristic frequency of the upper subband was within a few tenths of an meV of $(\omega^2_{Ni})^{1/2}_{av}$ in each case, but the lower subband frequency was typically 1 meV greater than $(\omega^2_{Mn})^{1/2}_{av}$. This strongly supports a picture of the two subbands as owing to Ni and Mn excitations, respectively, with only a slight amount of mixing. The second moment is sensitive to states at high energies. Admixture such that the amplitudes of the spin deviations on Ni sites are roughly 1% of those on the Mn sites, when averaged over the lower subband, is sufficient to cause the observed difference between the lower subband characteristic frequency and $(\omega^2_{Mn})^{1/2}_{av}$. A comparable admixture of Mn in the upper subband modes is presumed to occur, but will have no observable effect on the characteristic frequency.

The usual result for the strong scattering limit, that the number of states in each subband is equal to the number of atoms from which the subband was derived, need not hold in this system, since the density of states between the subbands is not strictly zero. However, we examined 64-by-64 samples with gaps as small as 1 meV (at $x=0.15$) and found in all cases that the number of states in each subband was equal to the number of the appropriate type of atoms on the resonant sublattice.

In Fig. 3(d), the light line shows, for comparison, the density of states of a pure Rb_2NiF_4 sample the same size as the Monte Carlo samples. Adding 10% Mn is seen to broaden the peak at the top of the band, and create a sharp resonance at low energies. Although there is no gap at this concentration, there appears to be a decrease in the density of states just above the resonance.

Cowley and Buyers,[2] among others, have analyzed the high-frequency excitations of this class of antiferromagnets using an Ising cluster approximation. The approximation consists of neglecting the terms in Eq. (1) involving S^x and S^y. Then the excitation energy for a unit spin excitation will depend only upon the atomic character of its nearest neighbors:

$$\Delta E_i = 2\sum_j J_{ij} S_j \,. \tag{42}$$

For Ni atoms surrounded by 0–4 Mn neighbors, the excitation energies given by Eq. (42) are 33.2, 30.8, 28.3, 25.8, and 23.3 meV, respectively, and in this picture they would enter the density of states weighted by the respective probabilities of finding that number of Mn nearest neighbors.

Since the Ising Hamiltonian lacks those terms which mix spin excitations on adjoining sites, this approximation is perhaps best viewed as the first of a series of approximations to localized spin excitations. Perturbations starting from this picture will broaden the Ising levels downward in energy,[23] with those excitations which are most extended in space lowered the most in energy.

This model has no relevance to the low-lying Mn modes, but we can find some support for it in the upper subband densities of states shown in Figs. 3(a) and 3(b). The peaks at 23.5 and 25.5 meV in Fig. 3(a) correspond to the energies of likely Ising clusters, and both peaks are still evident in Fig. 3(b). However, the cluster picture

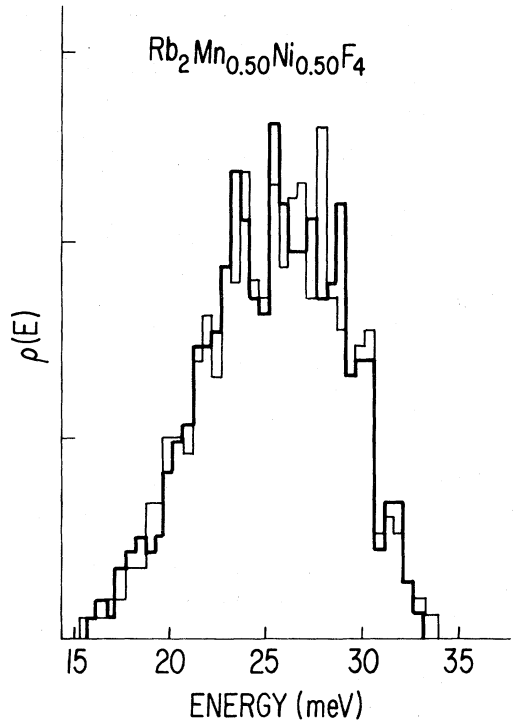

FIG. 4. Density of states in the upper subband at $x = 0.5$, for two Monte Carlo samples, results superimposed. One vertical division represents half as many states as in Figs. 3(a)–3(c).

would predict that the 25.5 peak should be twice as large as the 23.5 peak in the sample with Ni concentration of 0.35, while, in fact, it is somewhat smaller. This could reflect the fact that excitation of a single Ni spin surrounded by Mn atoms comes closer to being a true excitation of the system than does a mode which involves one Ni atom but not its Ni neighbor.

To check the reliability of interpretations based on peaked structures in these Monte Carlo densities of states, we repeated the calculation of the upper subband in another nearly equal concentration sample. The two results are compared in Fig. 4. The most apparent features, such as the sharp shoulder at 30.5 meV and the tail in the density of states below 20 meV, are well reproduced, but the spikes appear subject to small shifts, and may not be observable in crystals of macroscopic dimensions. However, the modes at 23.5 and 25.5 meV do survive averaging over the two cases in Fig. 4.

The rather different appearance of the two subbands in Figs. 3(a)–3(c) suggests that spatial characteristics of the states will be different in the two subbands. In all three of Figs. 3(a)–3(c), the lower subband has the characteristic shape of a band of 2D antiferromagnetic magnons, such as that plotted in Fig. 3(d). The curves are smooth, and each is peaked at higher energies. The upper subbands in Figs. 3(a) and 3(b) are roughly symmetric, and spiky. In Fig. 3(c), where the Ni concentration is 0.65, the spikes are less evident, and the density of states is shifting to higher energies within the band. Spiky densities of states like those in Figs. 3 and 4 have been observed in the strong-scattering limit in many other types of disordered systems, and are usually associated with localized eigenstates.[24,25]

An indirect measure of the degree of localization of an eigenstate, first suggested by Thouless,[26] is the sensitivity of the corresponding eigenvalue to a change from periodic to antiperiodic boundary conditions. States whose extent is less than the sample dimensions are not affected by this change, while the energies of extended states may shift by as much as the typical spacing between eigenvalues, in our examples, a few hundredths meV. The test ceases to be useful when the density of states per unit energy exceeds the inverse of the resolution with which eigenvalues can be determined. In our examples, this could occur only within 0.5 meV of the top of a band of extended magnons.

We applied this test at approximately 30 points each in the spectra of an $x = 0.5$ and an $x = 0.1$ sample. In the $x = 0.5$ sample, seven states below 5 meV were studied; all showed energy shifts between 6×10^{-3} and 2×10^{-2} meV, as would be expected for extended states. The shifts decreased monotonically between 5 and 6.5 meV. Above 6.6 meV, no eigenstates shifted by more than 2×10^{-4} meV, indicating that the states in the upper subband as well, are indeed localized. Localization at the top of the lower subband is not unexpected, since Mn spin excitations can have energies greater than 6.5 meV only with Ni atoms as neighbors. This is apparent from the formation of localized shell modes at these energies in the low-concentration limit. Since Ni spins at $x = 0.5$ occur in isolated clusters, these Mn modes can be localized.

The results for the $x = 0.1$ sample were more complicated. Only states with energies below 21 meV were tested. All states studied at energies below 6.1 meV or above 16 meV appeared to be extended. Three states between 11.6 and 15 meV proved relatively insensitive; their energies shifted by $(1-5) \times 10^{-3}$. The six states studied between 6.6 and 11.6 meV, a region comprising the top of the Mn resonance and the dip just above it, shifted less than 2×10^{-4} meV when boundary conditions were reversed. Ordinarily, one would expect that this strong a modification of the host band wave function would only occur for impurity concentrations greater than some threshold value x_c, and that below this threshold the Mn spins will act independently. But the very large size of the Mn

bound state found at low concentrations suggests that, in this case, $x_c < 10^{-4}$.

We did not find clear evidence in our calculations for the vanishing points[27] or blocked states discussed by Eggarter and Kirkpatrick,[25] but it is possible that our samples were too small, or our resolution too broad, to observe this.

III. STATIC AND LOW-TEMPERATURE PROPERTIES

In this section we sketch a continuum theory of the low-frequency, long-wavelength excitations which yields a description of these modes in terms of static response functions. In the absence of anisotropy, this derivation gives a consistent expansion in the small quantities q and ω, and is equivalent to the hydrodynamic treatment of Halperin and Hohenberg.[28] In this limit the expressions derived are valid at arbitrary temperatures. When anisotropy is present, all magnon frequencies are finite, a consistent expansion in powers of q and ω is not possible, and our results are approximate. However, corrections to the theory are of order the ratio of an anisotropy field to an exchange field, both of which will be defined below, and this ratio is less than 0.01 for the $Rb_2Mn_xNi_{1-x}F_4$ system.

Our starting point is a macroscopic expression for the increase in energy ΔE,

$$\Delta E = \frac{A}{4S_{\rm av}^2}\int d^3r \sum_{\alpha=x,y}\{\vec{\nabla}[S_a^\alpha(\vec{r}) - S_b^\alpha(\vec{r})]\}^2 + \frac{K}{S_{\rm av}^2}\int d^3r \sum_{\alpha=x,y}[S_a^\alpha(\vec{r})^2 + S_b^\alpha(\vec{r})^2] + \frac{\xi}{2S_{\rm av}^2}\int d^3r \sum_{\alpha=x,y}[S_a^\alpha(\vec{r}) + S_b^\alpha(\vec{r})]^2 , \tag{43}$$

due to components of spin deviation $S_a^\alpha(\vec{r})$ and $S_b^\alpha(\vec{r})$ per unit volume, on the a and b sublattices. $S_{\rm av}$, which denotes the macroscopic average magnitude of the spin density, is assumed to be the same on the two sublattices and independent of position. In a pure system, $S_{\rm av} = NS/2V$. A, K, and ξ are macroscopic magnetic elastic constants: A is the exchange stiffness,[39] K a uniaxial anisotropy energy, and ξ, which describes the exchange coupling between sublattices, is related below to the uniform static susceptibility.

Equations of motion for any Fourier component of $\vec{S}(\vec{r})$ are obtained by using ΔE as an effective Hamiltonian and treating the averaged spins as spin operators in the commutation relation,

$$i\hbar\frac{d\vec{S}(\vec{r})}{dt} = [\Delta E, \vec{S}(\vec{r})] . \tag{44}$$

For spins restricted within a manifold of g degenerate crystal-field levels, the spin to be used in (44) is the effective spin defined by $2S_{eff} + 1 = g$.[29] From the resulting equations of motion

$$\hbar\omega S_a^+(q) = (2/S_{\rm av})[(Aq^2/4 + K + \xi/2)S_a^+(q) + (\xi/2 - Aq^2/4)S_b^+(q)] , \tag{45a}$$

$$\hbar\omega S_b^+(q) = -(2/S_{\rm av})[(\xi/2 - Aq^2/4)S_a^+(q) + (Aq^2/4 + K + \xi/2)S_b^+(q)] \tag{45b}$$

the dispersion relation

$$[\hbar\omega(q)]^2 = S_{\rm av}^{-2}[2A\xi q^2 + 4K(K+\xi)] \tag{46}$$

is extracted.

To put Eq. (46) into a more familiar form we relate ξ to a susceptibility by adding to ΔE a term describing the interaction with a uniform field, $h_0\hat{x}$:

$$\Delta E^{\rm ext} = -\mu_B h_0 \int d^3r[S_a^x(\vec{r}) + S_b^x(\vec{r})] . \tag{47}$$

The equilibrium values of S_a^x and S_b^x, calculated by minimizing the sum of Eqs. (43) and (47), are

$$S_a^x = S_b^x = \mu_B h_0 S_{\rm av}^2/2(K+\xi) . \tag{48}$$

If we define

$$\chi^{\rm ss} = \mu_B(S_a^x + S_b^x)/h_0 , \tag{49}$$

we obtain

$$\xi = (\mu_B S_{\rm av})^2/\chi^{\rm ss} - K . \tag{50}$$

Using Eq. (50), the dispersion relation (46) is expressed as

$$\omega^2(q) = \omega_0^2 + C^2q^2 , \tag{51}$$

where

$$\omega_0 = (2\mu_B/\hbar)(K/\chi^{\rm ss})^{1/2} , \tag{52}$$

$$C = (1/\hbar)[2A(\mu_B^2/\chi^{\rm ss} - K/S_{\rm av}^2)]^{1/2} , \tag{53}$$

and in the absence of anisotropy,

$$C = (\mu_B/\hbar)(2A/\chi^{\rm ss})^{1/2} . \tag{54}$$

Expressions for the gap frequency ω_0 in terms of anisotropy and exchange fields are obtained by defining

$$H_A = 2K/M , \tag{55}$$

$$H_E = \xi/M , \tag{56}$$

where M is the magnitude of the magnetic moment per unit volume, from spins of one sublattice, and

$$\gamma_{\text{eff}} = M/\hbar S_{\text{av}} , \tag{57}$$

to yield the usual expression

$$\omega_0 = \gamma_{\text{eff}}[H_A(2H_E + H_A)]^{1/2} . \tag{58}$$

The above derivation in terms of spin densities differs slightly from the completely classical treatment of an antiferromagnet reported in Ref. 18, which considered the dynamics of the magnetization density. The present treatment avoids ambiguity in the definition of γ_{eff} in cases, such as $Rb_2Mn_xNi_{1-x}F_4$, in which components with different g values are present. Neither g nor γ appears in Eqs. (43)–(54). If we take γ in the expressions of Ref. 18 to be given by Eq. (57), the results of that paper are identical to the present work.

A consequence of the fact that the dynamics does not involve g factors is that the susceptibility which affects low-frequency modes is not the same as the susceptibility measured by applying an external field. The susceptibility defined by Eqs. (18) and (19) can be reduced to χ^{ss} by setting all g factors equal to unity. Thus we define the generalized spin-spin susceptibility as

$$\chi^{ss}(\vec{q}, \omega) = -2\langle \vec{q}^{\,s} | \underline{N}^{-1}(\omega) | \vec{q}^{\,s} \rangle , \tag{59}$$

with

$$\langle i | \vec{q}^{\,s} \rangle = \mu_B (S_i/V)^{1/2} e^{i\vec{q}\cdot\vec{R}_i} , \tag{60}$$

and χ^{ss} in Eqs. (49)–(54) is identified as $\chi^{ss}(0, 0)/2$. [The factor of 2 arises because $\chi^{ss}(\vec{q}, \omega)$ is defined as χ, instead of χ^{+-}.]

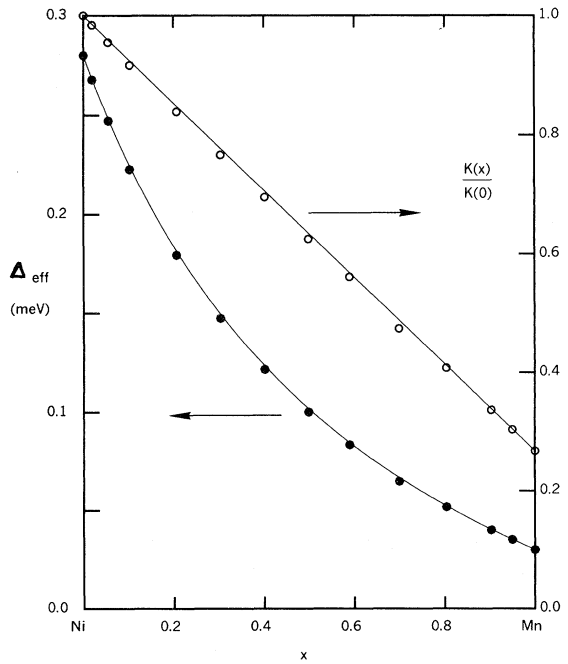

FIG. 5. Relative anisotropy constant $K(x)/K(0)$ (right-hand vertical scale) and anisotropy energy Δ_{eff}, defined as $2K(x)/S_{\text{av}}$ (left-hand scale), as function of concentration.

At the nuclear zone center ($\vec{q} = 0$), χ^{ss} is determined by the macroscopic quantities S_{av}, H_E, and K. Likewise, in the vicinity of the magnetic zone center $\vec{Q}$, where $e^{i\vec{Q}\cdot\vec{R}_i} = \sigma_i$, χ^{ss} can be expressed in terms of S_{av}, K, A:

$$\chi^{ss}(\vec{Q} + \vec{q}^{\,*}, 0) \sim 4\mu_B^2 S_{\text{av}}^2/(2K + Aq^{*2}) . \tag{61}$$

Equation (61) was used to calculate K and A as functions of x for the Monte Carlo samples. From $\chi^{ss}(\vec{Q}, 0)$, the staggered susceptibility, we obtained K. Then the slope of $\chi^{ss}(\vec{Q} + \vec{q}^{\,*}, 0)^{-1} - \chi^{ss}(\vec{Q}, 0)^{-1}$, when plotted against q^{*2}, determined A. The numerical procedures used to obtain χ^{ss} are described in Appendix A.

In the $Rb_2Mn_xNi_{1-x}F_4$ system, K should depend nearly linearly upon concentration. To zeroth order in H_A/H_E, the spins respond to a staggered field of the form (47) by rotating uniformly, and K is the average of the Mn and Ni values:

$$K(x) \sim xK_{\text{Mn}} + (1 - x)K_{\text{Ni}} . \tag{62}$$

Higher-order terms represent relaxation to a nonuniform response, which decreases ΔE and K by trading off anisotropy energy for exchange energy, but this effect is small when $H_A \ll H_E$. The exact limiting slope, $-K^{-1}dK/dc$, for x close to 0 or 1 is 13% greater than that given by Eq. (62) when small concentrations of Mn are added to Rb_2NiF_4, and 4% less than Eq. (62) predicts for Ni added to Rb_2MnF_4. This calculation is summarized in Appendix B. As expected, calculated values of $K(x)$, shown in Fig. 5, lie only slightly below the straight line connecting the two end points.[30]

The Monte Carlo data for concentrations within 10% of the end points of Fig. 5 agree with the low-concentration predictions. At intermediate concentrations, however, Eq. (62) is more accurate.

For the exchange stiffness $A(x)$, the approximations of assuming that the gradient of spin density remains uniform on the local scale and neglecting the anisotropy terms lead to

$$A(x) \sim x^2 A_{\text{Mn}} + 2x(1 - x)(A_{\text{Mn}} A_{\text{Ni}})^{1/2} + (1 - x)^2 A_{\text{Ni}} , \tag{63}$$

where we have made use of Eq. (3). Effects of local relaxation about the uniform response are more important in $A(x)$ than in $K(x)$, because variations in exchange energy from site to site are an appreciable fraction of the average exchange energy. As with $K(x)$, local relaxation to a lower-energy arrangement of spins depresses A below the uniform theory result (63), as the results in Fig. 6 show. The relative decrease due to relaxation is largest, although only 6–8%, in the concentration range from $x = 0.3$ to 0.6. This is to be expected, since the fluctuations which accompany the breakup of the stiff infinite

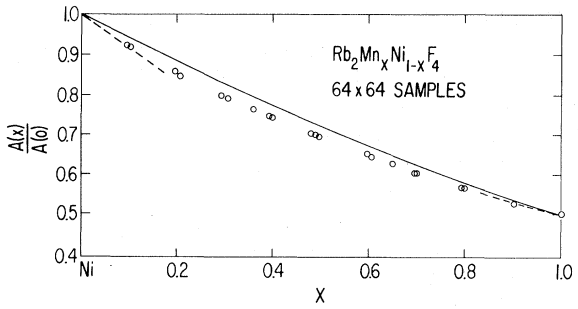

FIG. 6. Exchange stiffness constant $A(x)/A(0)$ normalized to the value for Rb_2NiF_4, calculated from $\chi^{ss}(\vec{Q}+\vec{q}^*, 0)$, as described in the text. Solid line gives the approximation to $A(x)/A(0)$ defined in Eq. (63). Dashed lines show the limiting slopes calculated from the exact single-defect solution.

Ni cluster will have an important effect on $A(x)$, while the formation of an infinite soft Mn cluster is not a dramatic change in the already soft material. At the Mn-rich end, for $x>0.75$, the uniform approximation is accurate to better than 3%. Because the ratio of the endpoints, $A(0)/A(1)$, is only a factor of 2, the amount of bowing seen in Fig. 6 in both the approximate and the calculated stiffness is relatively slight.

The limiting slopes of $A(x)$ at $x=0$ or 1 were calculated from the low-concentration results for $\chi(\vec{q}, 0)$, keeping terms to first order in H_A/H_E. The details of this calculation are summarized in Appendix B. The calculated values of $-A^{-1}(dA/dx)$, as indicated by the dashed lines in Fig. 6, were 0.827 at the Ni-rich end ($x=0$), and 0.691 at the Mn-rich end ($x=1$). Both are in good agreement with the Monte Carlo results. The curvature of the data away from its limiting slope is much greater at the Ni-rich end, as is expected from the arguments introduced above: soft inclusions in a stiff matrix will cause larger local relaxation effects than stiff inclusions in a soft matrix.

The perpendicular susceptibility, $\chi_\perp$, giving the response to a uniform external field, i.e., $\chi(0, 0)$ as calculated from (18), is shown by the solid-circle data points in Fig. 7. As was done with $A(x)$, we can obtain a simple approximation to $\chi(0, 0)$ by neglecting local relaxation and assuming that all Ni spins rotate by the same angle, θ_{Ni}, and all Mn spins by θ_{Mn}, in response to a uniform applied field. The expression for $\chi(0, 0)$ which results from minimizing the average energy under this assumption can be expressed in terms of the values at the Mn and Ni endpoints if we make use of Eq. (3):

$$\chi(0,0)=\frac{(xg_{Mn}S_{Mn}-yg_{Ni}S_{Ni})^2+2xyS_{Mn}S_{Ni}(\alpha g_{Ni}^2+\alpha^{-1}g_{Mn}^2)}{(xg_{Mn}S_{Mn}\chi_{Mn}^{-1/2}+yg_{Ni}S_{Ni}\chi_{Ni}^{-1/2})^2}\,, \tag{64}$$

where $\alpha=(J_{MnMn}/J_{NiNi})^{1/2}$, and $y=1-x$. The upper solid line in Fig. 7 is the result of applying Eq. (64) to $Rb_2Mn_xNi_{1-x}F_4$. Local relaxation causes a shift upwards in this response function, since the elastic energy is proportional to χ^{-1}. The extent of the bowing is greater in Fig. 7 than in Fig. 6 for two reasons. First, the endpoints are further apart. Second, at intermediate concentrations, there will be regions in which the net spin on the two sublattices does not cancel and the material will respond locally to a field as a ferrimagnet,[31] rather than as an antiferromagnet.

To separate the effects of the ferrimagnetic fluctuations, we have calculated $\chi_\perp$ for a hypothetical alloy with the same parameters J and Δ as $Rb_2Mn_xNi_{1-x}F_4$, but with $g=2$ and $S=1$ for both atomic species. For this material, the net torque on the system is always locally zero, and only the stiffness of the spin system fluctuates. The resulting susceptibility, plotted against concentration as crosses in Fig. 7, bows downward, and agrees with its corresponding virtual crystal prediction about as closely as did $A(x)$ in Fig. 6. The much larger upwards relaxation and scatter in the data points for the true $\chi(0, 0)$ is clear evidence for the strong response of local ferrimagnetic fluctuations. The effect is greatest near the percolation threshold for Mn, the component with the greater spin and weaker exchange interactions. This type of fluctuation does not have a strong effect on the values of A or K. Although in the ordered system one can write A, K, and $\chi_\perp$ in terms of H_E and H_A, in the disordered system the three quantities become independent. This difference is most marked in dilute antiferromagnets, where $\chi_\perp$ diverges at the percolation threshold.[18,31]

A low-concentration calculation of $\chi_\perp(x)$, which gives the limiting slopes indicated by dashed lines in Fig. 7, is summarized in Appendix B. Unlike the "averaged medium" arguments which were used to derive Eq. (64), this treatment includes (to lowest order) the effects of ferrimagnetic fluctuations. In particular, it predicts the increase in $\chi_\perp$ on adding Ni to $RbMnF_4$, which is seen in Fig. 7. The range of validity for the low-concentration treatment of the Ni-rich end is quite small, as we argued above in discussing the very-large bound state formed by Mn impurities. At the Mn-rich end, Fig. 7 shows that the limiting slope agrees with the data over a larger range of concentrations.

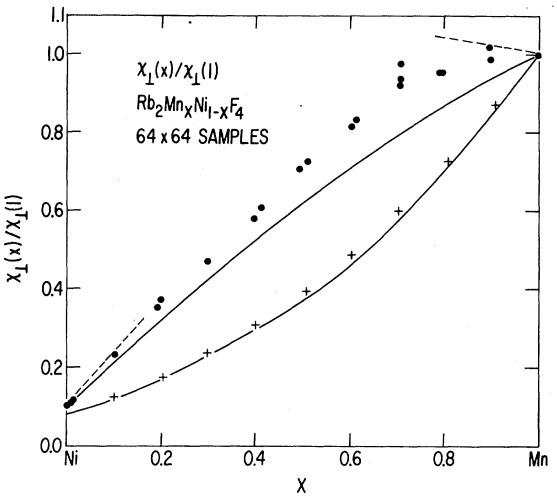

FIG. 7. Perpendicular susceptibility $\chi_\perp(x)/\chi_\perp(1)$ (solid circles) for several 64-by-64-site samples of $Rb_2Mn_xNi_{1-x}F_4$. Crosses represent $\chi_\perp(x)/\chi_\perp(1)$ for a hypothetical material without ferrimagnetic fluctuations, derived from $Rb_2Mn_2Ni_{1-x}F_4$ by setting $S=1$ and $g=2$ for all atoms. Solid lines show the prediction of the virtual crystal approximation (64) for these two cases, while dashed lines give the limiting slopes for the actual $\chi_\perp$ calculated from low-concentration theory. The two cases are normalized to unity at $x=1$, in contrast to Figs. 5 and 6, since both have the same magnitude at that point.

Calculation of χ^{ss} gave results similar to Fig. 7, although the bowing was more extreme. At concentrations between $x=0.5$ and 0.9, χ^{ss} slightly exceeded its value at the endpoint $x=1.0$. This type of concentration dependence for an elastic constant can only occur through the effects of those fluctuations (e.g., in S_i or g_i) which affect the coupling to the external field. It is absent, for example, in the virtual crystal approximation to χ^{ss}, obtained from Eq. (64) by setting all g's equal to unity. We can use χ^{ss} and $K(x)$ to predict the gap frequency, via (52). This prediction is compared in Fig. 8 with the only available experimental data, from the work of Birgeneau *et al.*,[3] and with the lowest eigenvalue found in our 64-by-64-site Monte Carlo samples at several concentrations. As mentioned above, the lowest-lying state in our simulations was always found to be an extended state. Its frequency is therefore a good approximation to the frequency of the $\vec{q}=0$ extended mode in the infinite system. The predictions are higher than the observations in all cases, with the error increasing as the gap frequency increases toward the Ni-rich end, but the discrepancy is never more than 0.3 meV. Such a discrepancy is expected, since our procedure of calculating the effective value of the quotient of two response functions as the quotient of their effective values is strictly valid only in the limit of vanishing q and ω. The gap frequency can be measured quite accurately by antiferromagnetic resonance, an experiment which would provide a valuable test of the present theory.

The continuum theory of this section can also be applied to calculate the temperature dependence of the sublattice magnetization. From the basic expressions (43) we can evaluate $\Delta S(T)/S_{\rm av}$, where $\Delta S(T) = S_{\rm av}(0) - S_{\rm av}(T)$. The continuum-theory results given in Eqs. (51)–(53) are restricted to the case $H_A \ll H_E$. In this limit, all spins precess in phase in the low-frequency modes, so that $\Delta M(T)/M \sim \Delta S(T)/S_{\rm av}$. Since

$$S_a^z(\vec{r}) = [S_{\rm av}^2 - S_a^x(\vec{r})^2 - S_a^y(\vec{r})^2]^{1/2}\,, \tag{65}$$

we can evaluate ΔS by expanding (65) for small S^x and S^y and, assuming isotropy in x and y,

$$\begin{aligned}\Delta S/S &= S_{\rm av}^{-2}\langle S_a^x(\vec{r})^2\rangle \\ &= (1/2\,S_{\rm av}^2)\langle S_a^x(\vec{r})^2 + S_b^x(\vec{r})^2\rangle\,,\end{aligned} \tag{66}$$

where $\langle\ \rangle$ denotes a thermal expectation value. Then

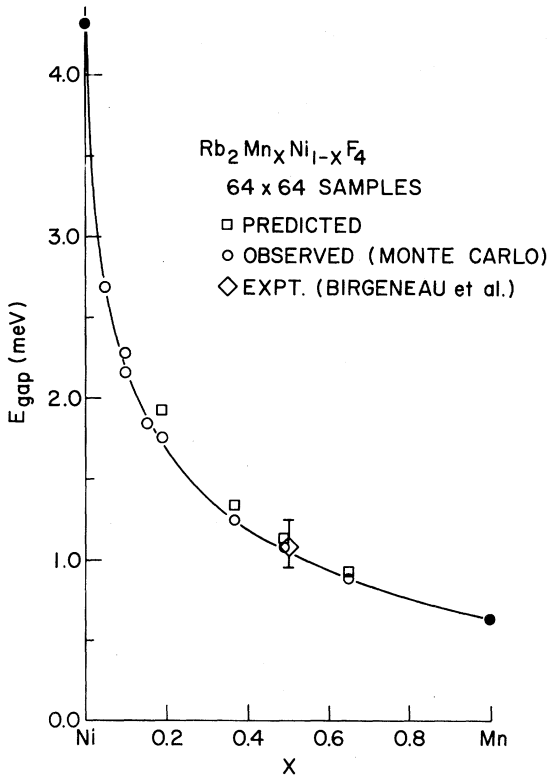

FIG. 8. Gap energy $F_g(x)$ as predicted from the static properties $\chi^{ss}(x)$ and $K(x)$, using Eq. (52) (squares), and as observed in Monte Carlo simulations (circles) and, for $x=0.5$, by inelastic neutron scattering (diamond). The solid line is drawn through the observed points as a guide to the eye.

$$\frac{\Delta S}{S} = \frac{1}{2S_{av}^2} \sum_{\vec{q}} \langle |S_a^x(\vec{q})|^2 + |S_b^x(\vec{q})|^2 \rangle \tag{67}$$

$$= (2S_{av})^{-2} \sum_{\vec{q}} \langle |S_a^x(\vec{q}) + S_b^x(\vec{q})|^2 + |S_a^x(\vec{q}) - S_b^x(\vec{q})|^2 \rangle . \tag{68}$$

For continuum variables we shall use the following definitions of the Fourier transform:

$$S_a^x(\vec{q}) = V^{-1} \int d\vec{r}\, S_a^x(\vec{r}) e^{-i\vec{q}\cdot\vec{r}} , \tag{69a}$$

$$S_a^x(\vec{r}) = \sum_{\vec{q}} S_a^x(\vec{q}) e^{i\vec{q}\cdot\vec{r}} , \tag{69b}$$

where V is the volume of the system. Because fluctuations of $S_a + S_b$ are of high energy, we can neglect $\langle |S_a^x + S_b^x|^2 \rangle$, and obtain

$$\frac{\Delta S}{S} = (2S_{av})^{-2} \sum_{\vec{q}} \langle |n(\vec{q})|^2 \rangle , \tag{70}$$

in which

$$n(\vec{q}) = S_a^x(\vec{q}) - S_b^x(\vec{q}) . \tag{71}$$

We distinguish the independent contributions of fluctuations in the real and imaginary parts of n:

$$\frac{\Delta S}{S} = (2S_{av})^{-2} \sum_{\vec{q}} \langle n'(\vec{q})^2 + n''(\vec{q})^2 \rangle \tag{72}$$

$$= \frac{1}{2S_{av}^2} \sum_{\vec{q}} \langle n'(\vec{q})^2 \rangle . \tag{73}$$

Since our macroscopic theory is not quantized, we shall use classical statistics to evaluate the amplitudes $\langle n'(\vec{q})^2 \rangle$. The energy of a fluctuation $n(\vec{q})$, obtained from Eq. (43), is

$$\Delta E(\vec{q}) = \frac{V}{4S_{av}^2} \sum_{\vec{q}} |n(\vec{q})|^2 (A\vec{q}^2 + 2K) . \tag{74}$$

Using Eq. (74), we obtain

$$\langle n'(\vec{q})^2 \rangle = \frac{\int dn'\, n'(\vec{q})^2 \exp\{-[2n'(\vec{q})^2/kT](V/4S_{av}^2)(Aq^2 + 2K)\}}{\int dn' \exp\{-[2n'(\vec{q})^2/kT](V/4S_{av}^2)(Aq^2 + 2K)\}} \tag{75}$$

$$= (kTS_{av}^2/V)(Aq^2 + 2K)^{-1} , \tag{76}$$

where we have used $n'(\vec{q}) = n'(-\vec{q})$ in Eq. (75). Substituting Eq. (76) into (73) we find

$$\frac{\Delta S}{S} = \frac{kT}{2V} \sum_{\vec{q}} (Aq^2 + 2K)^{-1} . \tag{77}$$

Using Eqs. (52) and (53) in the limit $H_A \ll H_E$, the spin-wave energies at low q are of the form

$$\hbar\omega(\vec{q}) = \Lambda(Aq^2 + 2K)^{1/2} . \tag{78}$$

Then Eq. (77) can be written

$$\frac{\Delta S}{S} = \frac{\Lambda^2}{2V} \sum_{\vec{q}} \frac{kT}{[\hbar\omega(\vec{q})]^2} . \tag{79}$$

We can now make contact with the usual quantum-mechanical expressions by identifying $kT/\hbar\omega(\vec{q})$ as a Bose occupation probability:

$$\frac{\Delta S}{S} \sim \frac{\Lambda^2}{2V} \sum_{\vec{q}} [\hbar\omega(\vec{q})]^{-1} (e^{\hbar\omega(\vec{q})/kT} - 1)^{-1} , \tag{80}$$

$$\frac{\Delta S}{S} \sim \frac{\Lambda^2}{4\pi c} \int q\, dq [\hbar\omega(q)]^{-1} (e^{\hbar\omega(q)/kT} - 1)^{-1} , \tag{81}$$

where c is the lattice constant perpendicular to the plane of spins. As long as Eq. (78) is valid, Eq. (81) can be evaluated exactly, and reduces to the same form[6] as that for a perfect 2D lattice:

$$\Delta M/M \sim \Delta S/S \sim -(kT/4\pi cA) \ln(1 - e^{-E_g/kT}) , \tag{83}$$

where E_g is the gap energy and cA is the exchange stiffness in units appropriate to a 2D system. For the planar square antiferromagnet, for example, $cA = JS^2$. Inserting this value of A into Eq. (83) gives the expression used by de Wijn *et al.*,[6] who have obtained good agreement between the prediction of this formula and the temperature dependence of the sublattice magnetization in K_2NiF_4 and K_2MnF_4.

In Fig. 9, we indicate the predictions of several approximations to $\Delta M(T)/M$ for the case $Rb_2Mn_{0.5}Ni_{0.5}F_4$. The dashed line was obtained by using the uniform approximation, Eq. (63), in Eq. (83). Introduction of the more accurate Monte Carlo value for $A(0.5)$ gives a further increase in the slope of $\Delta M(T)/M$, of about 10%. Experimental data on this system, obtained by Birgeneau *et al.*,[3] are plotted against $T\ln[1 - \exp(-E_g/kT)]$ in Fig. 9. As in the pure systems,[6] $\Delta M(T)/M$ proves to be linear on this scale at low temperatures. Both of our static approximations to $\Delta M(T)$ agree with the data to within experimental accuracy. The solid line, using the numerical calculation for A, appears to be in somewhat better agreement than the dashed line.

IV. EXCITATIONS AT HIGHER ENERGIES

The static response functions discussed in Sec. III are sufficient to characterize the extended states at low energies but contain no useful information about the excitations at higher energies, some of which may be localized. To study these states we have calculated the dynamic susceptibility $\chi(\vec{q}, \omega)$ for frequencies up to the highest magnon energies of Rb_2NiF_4, and $\vec{q}$ along the symmetry direction from (0, 0) to $\vec{Q} = (\pi/a, \pi/a)$, the magnetic zone center. Henceforth, in referring to a wave

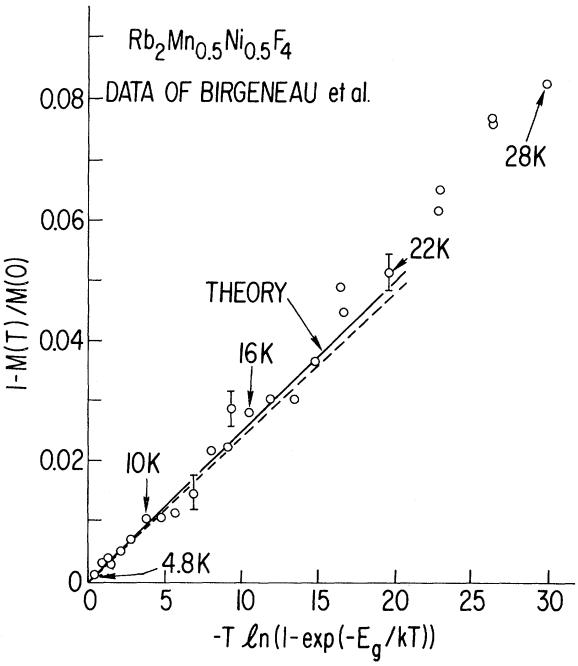

FIG. 9. Sublattice magnetization $M(T)$ as a function of temperature for $x=0.5$. Dashed line was obtained by using the result (83) of the long-wavelength theory and the uniform approximation (63) to $A(x)$. Solid line results from using the Monte Carlo results for $A(x)$ with (83). Data points were obtained from neutron-scattering intensities by Birgeneau *et al.*[3] (Ref. 3).

vector along this direction, we will use units of $\vec{Q}$:

$$\vec{q}=(q\pi/a,\ q\pi/a)\ . \tag{84}$$

The results can be directly compared with neutron scattering data, since the inelastic scattering intensity at momentum transfer q and energy transfer ω is proportional to $\chi''(q,\omega)$, the imaginary part of χ evaluated at an ω just off the real axis. In the work reported in this section, the imaginary part of ω was taken to be 0.2 meV, a value smaller than present experimental resolution, but large enough to eliminate the effects of the discrete spectrum of the 64-by-64-site samples studied.

Since χ'' is odd in ω, its even moments will vanish, on the average, but the average value of its odd moments can be evaluated exactly. The moments can be calculated in two ways. The Kramers-Kronig relation between χ' and χ'' requires that

$$\pi^{-1}\int d\omega\,\omega^{-1}\chi''(\vec{q},\omega)=\chi(\vec{q},0)\ . \tag{85}$$

In addition, a procedure of expanding $\underline{N}^{-1}$ and doing a contour integral, as in the derivation of (23), gives

$$(\hbar^2/\pi)\int d\omega\,\omega\chi''(\vec{q},\omega)=\langle\vec{q}|\underline{\sigma W\sigma}|\vec{q}\rangle\ , \tag{86}$$

$$(\hbar^4/\pi)\int d\omega\,\omega^3\chi''(\vec{q},\omega)=\langle\vec{q}|\underline{\sigma W\sigma W\sigma W\sigma}|\vec{q}\rangle\ . \tag{87}$$

Equations (85)–(87) were used as checks on our calculations. The data which will be plotted and discussed below satisfied them to 5% or better at all values of q.

By inserting projection operators, $P_{\rm Mn}$ and $P_{\rm Ni}$, to the left and right of the operators whose matrix elements are evaluated in Eqs. (86) and (87), we can evaluate moments of the partial susceptibilites, $\chi''_{\rm MnMn}(\vec{q})$, $\chi''_{\rm MnNi}(\vec{q})$, and $\chi''_{\rm NiNi}(\vec{q})$. Just as was done in studying the subbands of the density of states, it is possible to obtain characteristic energies for the excitations associated with a given type of atom which scatter at wave vector $\vec{q}$. Since high energies dominate the moments defined in Eqs. (86) and (87) this procedure is most useful for the Ni subband. We shall define a characteristic energy for Ni

$$\omega_{\rm Ni}(\vec{q})=\{[\omega^3_{\rm NiNi}(\vec{q})]_{\rm av}/[\omega_{\rm NiNi}(\vec{q})]_{\rm av}\}^{1/2}=\frac{\left(\int d\omega\,\omega^3\chi''_{\rm NiNi}(\vec{q},\omega)\right)^{1/2}}{\left(\int d\omega\,\omega\chi''_{\rm NiNi}(\vec{q},\omega)\right)^{1/2}}\ . \tag{88}$$

The terms which must be evaluated to use Eqs. (86)–(88) are derived in Appendix C and tabulated as (C7) and (C10).

The calculated total scattering intensities $\chi''(q,\omega)$ for the four concentration regimes studied are displayed in Figs. 10(a)–10(d). Each of the figures shows $\chi''(q,\omega)$ for 14 values of q between 0 and 1. The origins of the plots are shifted upwards in proportion to the magnitude of q. Although the vertical scale is in arbitrary units, all of the curves in the four figures are plotted to the same scale and may be compared against one another. Results were obtained at intervals of 0.5 meV.

Figure 10(a) shows the highest Mn concentration studied, $x=0.662$. The low-energy lines seen in Fig. 10(a) show the expected behavior for extended states in that the width of the peaks is limited by the imaginary part added to ω and the intensities increase smoothly as q increases towards 1. The Ni states between 16 and 32 meV appear to be strongly localized. These lines are all 4–8 meV wide, depending upon how the width is defined, and the peak centers shift with q over an amount which is less than this width. The characteristic frequency $\omega_{\rm Ni}(q)$ is plotted as a vertical solid line on each of the upper subband scattering intensities. It gives an accurate estimate of the position of the upper subband peaks. Fingally, we note that the line widths are insensitive to q in both subbands.

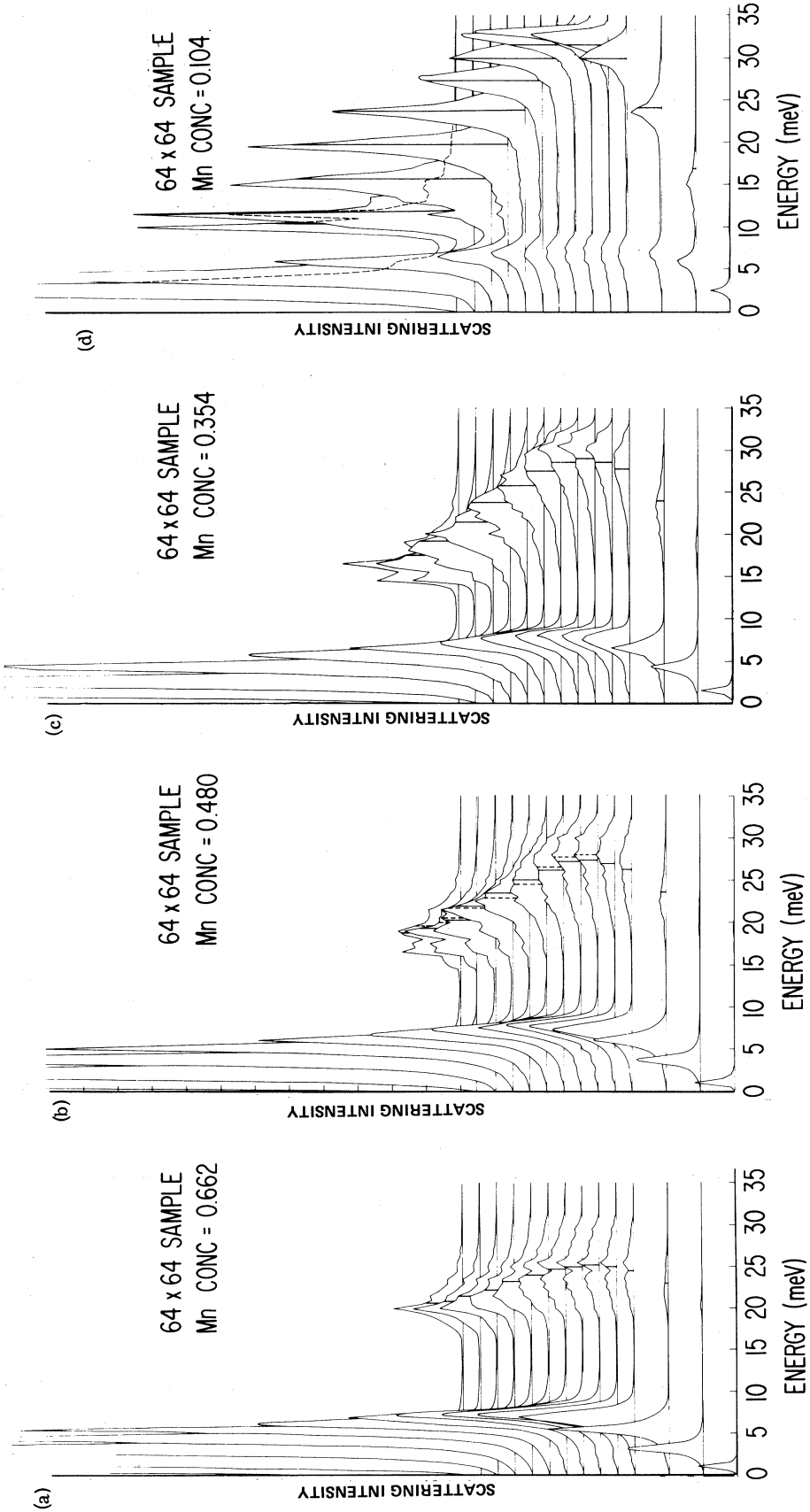

FIG. 10. Inelastic-neutron-scattering cross section $\chi''(q,\omega)$ as a function of energy for 14 values of $\vec{q}$ along the symmetry direction from (0, 0) to $\vec{Q}=(\pi/a, \pi/a)$, at concentrations $x=0.662$ (a), 0.480 (b), 0.354 (c), and 0.104 (d). The values of q, in the units defined in (84), are, from bottom to top: 0, $\frac{1}{8}$, $\frac{1}{4}$, $\frac{3}{8}$, $\frac{7}{16}$, $\frac{1}{2}$, $\frac{9}{16}$, $\frac{5}{8}$, $\frac{11}{16}$, $\frac{3}{4}$, $\frac{13}{16}$, $\frac{7}{8}$, $\frac{15}{16}$, and 1. Vertical scales are the same for all curves. The baseline for each curve is shifted upwards by an amount proportional to q. Solid lines drawn upon some of the upper subband intensity plots indicate the characteristic frequency $\omega_{Ni}(q)$ deduced via (88) from the first and third moments of $\chi''_{NiNi}(q,\omega)$. Dashed lines in the upper subband plots of (b) indicate peak positions observed by inelastic neutron scattering in Ref. 3.

At a Mn concentration of 0.48, shown in Fig. 10(b), both the Mn and Ni lines are broader than in the previous case. The dispersion of the Ni peaks is now slightly greater than their width, yet it was shown in Sec. II that these states are well localized. Therefore, this rule of thumb for distinguishing localized from extended states is insufficient, at least in 2D. One can also infer from Fig. 10(b) that the Ni states are relatively large. A band of localized states confined to a few atomic sites each will get its width from the distribution of local environments which are encountered. The scattering of such states will occur at the same frequency for all q. In contrast, the upper subband of Fig. 10(b) must include states which have lowered their energies by spreading over large clusters. Large localized states of this type will scatter preferentially at q near a reciprocal lattice vector. Dean and Bird's observation[8] that, in a sample with $x = 0.5$, the average cluster contained eight sites is consistent with this interpretation.

Measurement of half-widths of the peaks near $q \sim 0.5$ indicates that the lines seen at concentrations for which either the Mn or the Ni atoms are connected in an infinite cluster [Figs. 10(a) and 10(c)] are narrower than those of Fig. 10(b). Also the apparently "propagating" Ni modes at $x = 0.5$ were shown in Sec. II to be localized. Both of these observations are consistent with our intuition that the intermediate regime, in which the underlying lattice consists only of isolated clusters, should be the most disordered.

The calculation in Fig. 10(b) is in agreement with the neutron scattering data of Birgeneau *et al.*[3] The experimental peak positions are indicated on the upper subband scattering intensities with heavy dashed lines, and are within less than 0.5 meV of the characteristic frequency predicted from moments in each case. The lower subband peak positions also agree with those measured by neutron scattering. Our calculation for this case, and the calculations of Alben and Thorpe,[11] appear to agree down to the presence of similar fine structure in the upper subband intensities. This is to be expected since their calculations differ from the present one only in the numerical techniques employed.

In Fig. 10(c), for a Mn concentration of 0.354, the peaks in both subbands have developed an asymmetric shape, with long tails to lower energies. The upper subband lines are narrower than in Fig. 10(b). As the dispersion of this subband increases, and the peaks become skewed, $\omega_{\mathrm{Ni}}(q)$ becomes less accurate as an estimate of the mode energy. It is in error by as much as 1 meV at the extremes of the upper subband in Fig. 10(c). A lack of symmetry between the two subbands is evident in Figs. 10(a) and 10(c). Although both the Mn spins at $x = 0.662$ and the Ni spins at $x = 0.354$ occur in infinite clusters, the Ni subband states for $x = 0.354$ are more strongly affected by disorder than are the Mn subband states at $x = 0.662$. The Ni states are considerably broader than the Mn states, and show a spiky structure like that found in the density of states and discussed in Sec. II. The dissimilarity in these two cases can be related to their respective low-concentration limits. When x is close to 1, Ni addition leads to localized modes above the Mn band. At values of x close to 0, Mn impurities cause a low-energy resonance, but cannot localize the long-wavelength acoustic modes.

The most intriguing and complex case studied is $x = 0.104$, shown in Fig. 10(d). The Ni lines have narrowed further, and have the appearance of extended states, at least at the top of the spectrum, around $q = 0.5$. The Ni peak positions could be estimated with an accuracy of better than 1 meV from $\omega_{\mathrm{Ni}}(q)$, as would be expected for such narrow lines. The Mn subband scattering shows a constant width and nearly constant intensity from $q = 0.375$ to 0.625, as one would expect for strongly localized states. The calculations of the sensitivity of specific eigenvalues to changes in the boundary conditions, discussed in Sec. II, support this interpretation. The states which had filled in the gap just above the Mn resonance in the density of states shown in Fig. 3(d) can be seen in Fig. 10(d) to come from a small area of q space near the point Q (or, equivalently, 0). Even in the absence of a gap in $\rho(E)$, two-mode behavior is seen at all q. We shall discuss the gap states further below, in the light of the partial susceptibilities calculated for this case.

In Figs. 10(a)–10(c), there is structure in $\chi''(q, \omega)$ near $q = 0.5$, some, but not all, of which can be associated with the Ising resonances seen in the density of states and discussed in Sec. II. Such resonances will be more pronounced and easier to analyze in a dilute one-component system. They have previously been studied numerically for a dilute 3D antiferromagnet.[23]

In order to give a quantitative analysis of the Monte Carlo results displayed in Figs. 10(a)–10(d), we shall develop some analytic approximations for $\chi''(\vec{q}, \omega)$. The most useful of these is a generalization to arbitrary x of the four-sublattice model introduced in Ref. 3. This model is just an averaged medium approximation carried out at finite q and ω, and is similar in some respects to the "average t-matrix" approximation which has been used in the study of electrons in alloys.[13] One makes the Ansatz that the response of a spin on site i to a driving field $h_0 \exp(i\vec{q} \cdot \vec{R}_i - i\omega t)$ can have one of four values, $S_{\alpha\sigma} \exp(i\vec{q} \cdot \vec{R}_i - i\omega t)$, depending only on the type of atom at site i (α_i = Mn or Ni) and the sublattice ($\sigma_i = \pm 1$). To determine the

$S_{\alpha\sigma}(\vec{q}, \omega)$, one minimizes the average energy of the system (1) in the presence of the driving field. The linearized equations which result are

$$\sum_{\beta\tau} M^*_{\alpha\sigma\beta\tau}(\vec{q}, \omega) S_{\beta\tau}(\vec{q}, \omega) = -2g_\alpha \mu_B S_\alpha h_0 , \tag{89}$$

in which

$$M^*_{\alpha\sigma\beta\tau} = \delta_{\alpha\beta}\delta_{\sigma\tau}(d_\alpha + \hbar\sigma\omega) + (1-\delta_{\sigma\tau}) 2z\gamma(\vec{q}) J_{\alpha\beta} S_\alpha x_\beta , \tag{90}$$

where z is the number of nearest neighbors,

$$d_\alpha = \Delta_\alpha + 2zx J_{\alpha \mathrm{Mn}} S_{\mathrm{Mn}} + 2zy J_{\alpha \mathrm{Ni}} S_{\mathrm{Ni}} , \tag{91}$$

and for the 2D square lattice,

$$\gamma(\vec{q}) = \tfrac{1}{2}[\cos(q^x a) + \cos(q^y a)] . \tag{92}$$

In calculating $\chi(\vec{q}, \omega)$ it is in convenient to have a symmetric system of equations. This is achieved by defining

$$s_{\alpha\sigma}(\vec{q}, \omega) = (x_\alpha^{1/2} S_\alpha^{-1/2}) S_{\alpha\sigma}(\vec{q}, \omega) , \tag{93}$$

which satisfy

$$\sum_{\beta\tau} N^*_{\alpha\sigma\beta\tau}(\vec{q}, \omega) s_{\beta\tau}(\vec{q}, \omega) = -2g_\alpha \mu_B x_\alpha^{1/2} S_\alpha^{1/2} h_0 , \tag{94}$$

where the diagonal elements of $\underline{N}^*$ are the same as those of $\underline{M}^*$, and for $\sigma \neq \tau$,

$$N^*_{\alpha\sigma\beta\tau} = 2z\gamma(\vec{q}) J_{\alpha\beta}(x_\alpha x_\beta S_\alpha S_\beta)^{1/2} . \tag{95}$$

Averaging the response $S_{\alpha\sigma}(\vec{q}, \omega)$ over sublattice and type of atom gives for the dynamic susceptibility in this approximation

$$\chi(\vec{q}, \omega) = \frac{-2}{V} \sum_{\alpha\sigma\beta\tau} g_\alpha g_\beta \mu_B^2 (S_\alpha S_\beta x_\alpha x_\beta)^{1/2} (\underline{N}^{*-1})_{\alpha\sigma\beta\tau} . \tag{96}$$

The imaginary part of $\underline{N}^*(\vec{q}, \omega)^{-1}$ is evaluated in Appendix D, and will be used below in the discussion of the total and projected scattering intensities. It is not difficult to show that the real part of Eq. (96) reduces at $q=0$ in the static limit to the average medium expression for $\chi_\perp$ given in Eq. (64) and tested in Fig. 7. The approximation (63) for A can also be extracted from this theory.

The secular equation that results from inverting $\underline{M}^*$ or $\underline{N}^*$ and using Eq. (3) is

$$0 = \omega^4 - \omega^2[d^2_{\mathrm{Mn}} + d^2_{\mathrm{Ni}} - 4z^2\gamma(\vec{q})^2 (xJ_{\mathrm{MnMn}} S_{\mathrm{Mn}} + yJ_{\mathrm{NiNi}} S_{\mathrm{Ni}})^2] + d^2_{\mathrm{Mn}} d^2_{\mathrm{Ni}} - 4z^2\gamma(q)^2 (xJ_{\mathrm{MnMn}} S_{\mathrm{Mn}} d_{\mathrm{Ni}} + yJ_{\mathrm{NiNi}} S_{\mathrm{Ni}} d_{\mathrm{Mn}})^2 . \tag{97}$$

When Eq. (3) does not hold, the more general secular equation is easily obtained by setting the determinant Δ, calculated in Appendix D, equal to zero. This theory must be used with caution, since $\underline{N}^*(\omega)$ is not the average of a dynamical matrix for any actual arrangement of "effective" spins. Equation (97) gives reasonable results in some limits, and incorrect predictions in others. Thus, at $q=0.5$, all the terms involving γ in Eq. (97) vanish, leaving

$$\omega_1 = \pm d_{\mathrm{Mn}} , \quad \omega_2 = \pm d_{\mathrm{Ni}} , \tag{98}$$

which are the average for each type of atom of its Ising cluster energy levels. This is a quite reasonable result. At $q=0$ or 1, however, the frequency of the upper mode always exceeds d_{Mn}, so there is always a gap between subbands. In addition, in the absence of disorder, when all $J_{ij} = J$, and all $S_i = S$, the two modes are

$$\omega_1^2 = d^2 - 16\gamma(\vec{q})^2 J^2 S^2 , \tag{99a}$$

$$\omega_2^2 = d^2 , \tag{99b}$$

and ω_2 is spurious. However, the difficulty seen in Eq. (99) does not immediately rule out applying this model to a material in which the J_{ij}'s and S_i's differ considerably.

The mode frequencies predicted by the four-sublattice model are qualitatively correct, but not in quantitative agreement with the observed results plotted in Fig. 11. We have plotted the energies of the two modes at $q=1.0$ in this figure, since the presence or absence of an energy gap between the subbands depends primarily upon the energy of the upper mode at this point. The agreement is best in the lower subband. The difference between the four-subblatice prediction of the gap frequency and the value observed in our Monte Carlo calculations is roughly twice the error found for the predictions of the static theory, plotted in Fig. 8. The upper mode frequency, however, is seen to be 3–5 meV less than the prediction of the four-sublattice model, while the estimate from moments of the partial susceptibility is reasonably accurate. We were not able to obtain accurate estimates of $\omega_2(\vec{Q})$ from the moments at concentrations close to the Ni or Mn endpoints, because of the greater strength of the scattering from the lower subband. At the Ni endpoint, of course, $\omega_1(\vec{Q}) = \omega_2(\vec{Q}) = E_g$. At the Mn endpoint, the low-concentration theory of Sec. II was used to obtain the limiting value of ω_2 which is indicated

A stronger test of our physical picture of the two branches of excitations and of the four-sublattice theory is the calculation of scattering intensities, which depend sensitively upon wave functions. The absolute scattering intensities I_1 and I_2 from our Monte Carlo calculations, defined as

$$I_n = \frac{\hbar V}{N\pi} \int_{n\text{th subband}} d\omega \, \chi''(\vec{q}, \omega - i\epsilon) , \tag{100}$$

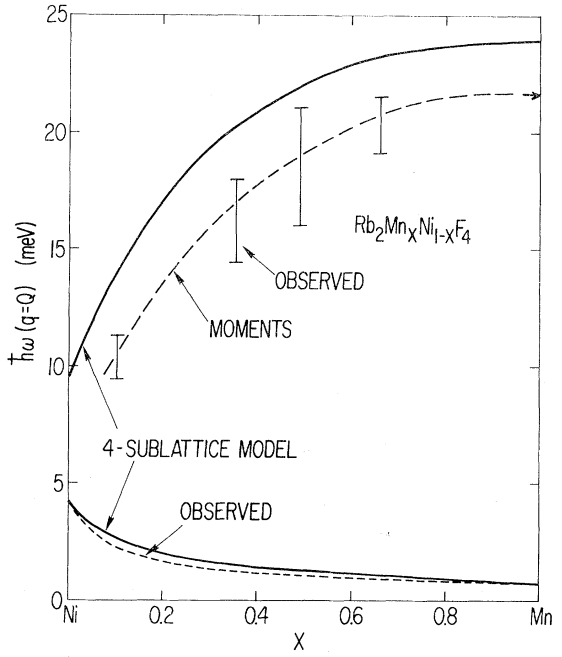

FIG. 11. Energies of the two modes at $\vec{Q}$, the magnetic zone center, as a function of x, as observed in 64-by-64-site Monte Carlo calculations (data bars denote half-maximum widths of the upper subband peaks, the short dashed line indicates the lowest eigenvalue, or gap frequency, from the simulations), are compared with prediction of the four-sublattice model (solid lines) and extrapolations from moments (long dashed line). Experimental data from Ref. 3 at $x=0.5$ agree with the observations plotted here [see Figs. 8 and 10(b)]. The arrow at the Mn-rich end of the upper mode indicates the energy of an isolated Ni spin in Rb_2MnF_4, as shown in Fig. 2(a).

are displayed as functions of q, normalized in appropriate ways, in Figs. 12(a) (lower mode) and 12(b) (upper mode). Since I_1 can be thought of as due to Mn spin excitations, we have used the scattering intensity per Mn spin in pure Rb_2MnF_4:

$$I_{\text{pure Mn}}(q) = g_{\text{Mn}}^2 \mu_B^2 S_{\text{Mn}} \frac{H_A + H_E[1-\gamma(q)]}{[(H_A+H_E)^2 - H_E^2\gamma(q)^2]^{1/2}} , \tag{101}$$

as a reference, and plot $I_{\text{lower}}(q)/xI_{\text{pure Mn}}$ in Fig. 12(a). In each case we find that the scattering intensity is decreased at intermediate values of q. The decrease is greatest, roughly 50%, for the most dilute sample studied, $x=0.104$, and least, about 20%, for the most concentrated, $x=0.662$.

At each concentration shown in Fig. 12(a), there is excess scattering in I_1 above this reference level for $q<0.25$. This occurs in part because the spin waves near $q=0$ are not just Mn excitations, but must involve both Mn and Ni spins, precessing in phase. The scattering intensity at $q=0$ is therefore proportional to $g_{\text{av}}^2 S_{\text{av}}$ instead of to $x_{\text{Mn}} g_{\text{Mn}}^2 S_{\text{Mn}}$. Including Ni participation in this way accounts for an enhancement of 5.6 times at $x=0.104$ (our calculations give a 7.3 times enhancement), 2.0 times at $x=0.35$ (2.8 is calculated), 1.6 times at $x=0.48$ (2.6 is calculated), and 1.4 times at $x=0.66$ (1.7 is calculated). The remaining enhancement may be due to ferrimagnetic fluctuations, or to fluctuations in g_i, both of which shift scattering intensity from the vicinity of Q to the vicinity of 0. The rolloff of intensity seen near $q=1$ in Fig. 12(a) is consistent with this interpretation.

Since the Ni-dominated upper mode consists primarily of localized states in several of the samples under study, we have plotted $I_{\text{upper}}(q)$ for the four cases [in Fig. 12(b)], normalized to the constant Ising cluster prediction, $yg_{\text{Ni}}^2 S_{\text{Ni}}$. In the upper mode, all the calculated intensities at intermediate values of q are higher than the scattering intensity per spin found in pure Rb_2NiF_4, which is shown with a dotted line in Fig. 12(b). The difference increases monotonically as the Ni concentration decreases.

Since the upper-mode frequency remains large

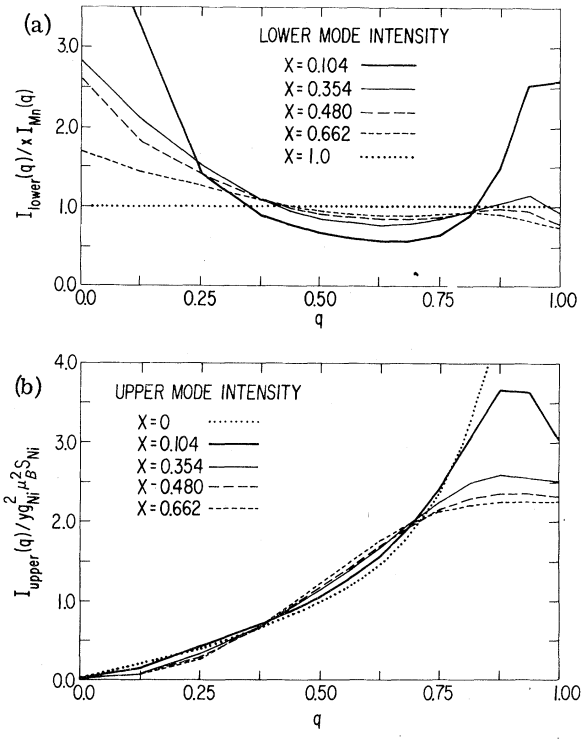

FIG. 12. Integrated scattering intensities in the upper and lower subbands as functions of q, for the four cases plotted in Figs. 10(a)–10(d). In (a) the lower subband intensities are plotted, normalized to the product of the Mn concentration and the scattering intensity expected for pure Rb_2MnF_4, as given in (101). Upper subband intensities, shown in (b), are normalized to the constant, $yg_{\text{Ni}}^2\mu_B^2 S_{\text{Ni}}$, the intensity predicted by the Ising cluster model.

at $q=0$ and 1, I_2 does not show the enhancement due to the factor $\omega(\vec{q})^{-1}$ in (101), which comes from coupling to the nonresonant sublattice. Instead, in all four cases, $I_2(0)/yI_{\text{pure Ni}}(0) \sim I_2(1)/I_{\text{pure Ni}}(1) \sim 0.2$. In Figure 10(a), which depicts $x=0.66$, the upper mode has almost no dispersion. We have compared $I_2(q)$ per Ni atom for this case with the scattering intensity for the localized resonance on an isolated Ni atom, as calculated in Appendix B. The two intensities are identical for $q>0.5$. As q tends to 0, the upper-mode intensity per Ni atom for $x=0.66$ was less than the isolated Ni limit, but the maximum error was 25%. This corroborates our observation above that localization has set in in the Ni subband by $x=0.5$. Since the scattering intensity has saturated by the time q is within 0.25 of the magnetic zone center, we conclude that localized states of greater extent than $(1-q)^{-1} \sim 4$ sites are probably rare. The most Ni-rich sample studied, $x=0.104$, showed the greatest variation in $I_2(q)$. I_2 increased to a maximum of 3.4 $I_2(0.5)$, just before the two modes merged at $q=1$, making separation of the intensity into I_1 and I_2 somewhat arbitrary.

Our calculated intensities are in fair agreement with the experimental data on $Rb_2Mn_{0.5}Ni_{0.5}F_4$ published by Birgeneau *et al.*[3] Although they did not measure absolute intensities, we can compare our calculations with their measured intensity ratios. For $I_2(q)/I_1(q)$ at $q=0.2$, 0.5, and 0.8, they obtained 0.47, 0.9 ± 0.2, and 0.58, while our calculations give 0.26, 0.7, and 0.44, respectively. The consistently larger ratios observed experimentally may be a consequence of spin-wave interactions. We found in Sec. II that the Ni modes are localized at this concentration, which implies relatively large spin deviations per atom in each mode. Since each such excitation will decrease the exchange stiffness felt by nearby spins, the net effect is an enhanced susceptibility. If this interpretation is correct, a similar, but smaller increase of intensity, due to these interactions in the lower subband, will be observed at low Mn concentrations, such as the $x=0.104$ case discussed above, when all the Mn states are localized and the Ni states extended for $q \sim 0.5$.

The scattering intensities of the two sharp modes within the four-sublattice model have qualitatively the same dependence on x and q as do the Monte Carlo integrated intensities, I_1 and I_2, shown in Figs. 12(a) and 12(b). Since this approximation is a simple one, we will discuss the limits of its accuracy in some detail. The intensity predicted by the four-sublattice model is larger than that observed in the lower subband, and smaller in the upper subband. The ratio of the model's intensities to the observed I_1 and I_2, however, is nearly constant over the range $0.25<q<0.75$, and can be obtained from Figs. 12(a) and 12(b), as discussed below.

First we consider the lower subband. At $q=0.5$ in the lower mode, the four-sublattice model gives spin deviations on Mn sites of the resonant sublattice only. Consequently, the predicted intensity is the Ising cluster intensity, and the amount by which the model overestimates $I_1(q)$ can be read off Fig. 12(a) by comparing the Monte Carlo results with the dotted line at $q=0.5$, where the dotted line is equal to the four-sublattice prediction. The discrepancy between this approximation and the Monte Carlo results decreases as q tends to 0 or 1, and the modes become more extended. The observed $I_1(0)$ and $I_1(1)$ reach 85%–95% of the four-sublattice prediction for all x studied. Most of the shift in intensity from the vicinity of $q=1$ to $q=0$ seen in Fig. 12(a) is predicted in this model as well.

In the upper subband we find that $I_2(q)$ exceeds the four-sublattice estimates by a constant 10%–25% for most values of q. The difference, which decreases with increasing Ni concentration, may be read off Fig. 12(b) by comparing the data with the dotted line at $q=0.5$. In the discussion below, we attribute this systematic overestimate by the four-sublattice model of the lower-mode intensity and underestimate of the upper-mode intensity to the fact that the model underestimates the net coupling between Ni and Mn spin deviations in the random system.

The partial susceptibilities $\chi''_{\alpha\beta}(q, \omega)$ were calculated for the $x=0.48$ sample at all frequencies, and for the $x=0.104$ sample at energies in the lower subband and the pseudogap, up to 14.5 meV. We can estimate the admixture of Ni states in the lower subband by comparing the integrals of $\chi''_{\text{NiNi}}(q, \omega)$ and $\chi''_{\text{MnMn}}(q, \omega)$ over that subband at values of $q \sim 0.5$. At $q=0.5$ this ratio is 3% in the $x=0.48$ sample, and 5% in the $x=0.104$ sample. It was no greater than 5% in both samples over the range $0.25<q<0.75$, which constitutes most of phase space in 2D. In the upper subband, for $x=0.48$, the integrated Mn intensity at $q=0.5$ in 6% of the Ni intensity, and remains less than 10% of the Ni intensity for $0.25<q<0.75$. This substantiates the interpretation of the two subbands as due largely to spin deviations on Mn and Ni sites, respectively.

The four-sublattice model does not treat these admixture effects correctly in the vicinity of $q=0.5$, since interactions between neighboring spins vanish at $q=0.5$ in the high symmetry of the averaged medium. The normal modes in the four-sublattice model at $q=0.5$ consist only of spin deviations on Ni or on Mn sites on the resonant sublattice. Thus the model predicts $\chi''_{\text{NiNi}}(0.5, \omega_1) = \chi''_{\text{MnNi}}(0.5, \omega_1) = 0$, and conversely, $\chi''_{\text{MnMn}}(0.5, \omega_2) = \chi''_{\text{NiMn}}(0.5, \omega_2)$

$=0$. The systematic differences in absolute intensities between the four-sublattice model and our observations seen in Figs. 12(a) and 12(b) are due to the underestimate of χ''_{MnNi} in the model. The contribution of this cross term to $I_1(0.5)$ in the Monte Carlo results at $x=0.48$ is negative and about 20% of the contribution from χ''_{MnMn}. In $I_2(0.5)$ for the same sample the cross-term contribution is positive, and about 7% of the Ni-Ni contribution. For the more dilute $x=0.104$ sample the cross term was again negative, reducing χ''_{MnMn} by more than 40%. The difference in sign between the two subbands can be explained by the fact that in the lower subband, the Ni spins are below their resonant frequency, and will tend to lag the driving Mn spins, while in the upper subband the Mn spins are above resonance, and will lead. This mixing, which vanishes by symmetry in the pure system, will not vanish in the presence of fluctuations, and accounts for the systematic trends in the intensities seen in Figs. 12.

V. CONCLUSIONS

We summarize our conclusions as follows

(i) The low-frequency behavior of mixed magnetic systems is conveniently formulated in terms of the static magnetic elastic constants, the exchange stiffness, the spin-spin susceptibility, and the anisotropy, in the context of a continuum theory which reproduces hydrodynamics in the limit of small anisotropy.

(ii) The concentration dependence of these magnetic elastic constants in mixed crystals can be qualitatively understood within an average medium theory which is equivalent to the "four-sublattice" model introduced by Birgeneau *et al.*[3] The ratio of the exchange fields of the two components in the system under study is not sufficiently different from unity for dramatic effects of the respective percolation thresholds to be observable, as they would be in a dilute one-component system.

(iii) The high-frequency excitations can usefully be simulated by exact solution of the dynamical equations of a large randomly prepared system. In the case of $Rb_2Mn_xNi_{1-x}F_4$, the Ising resonances are barely observable. It is clear from previous work[23] that these should be prominent in 2D alloys with one component nonmagnetic.

(iv) The partial susceptibilities and intensities calculated numerically agree qualitatively with results from the simpler four-sublattice model. The conditions under which this model can fail are discussed in Sec. IV.

(v) Low-concentration theory provides useful insight into the higher concentration behavior of mixed crystals, especially when the different types of spins have widely differing Ising excitation energies. The localized Ni modes seen in $Rb_2Mn_xNi_{1-x}F_4$ for $x>0.5$ are tightly bound to Ni clusters, and have properties very similar to those of isolated Ni spins.

(vi) In $Rb_2Mn_xNi_{1-x}F_4$, localization, as indicated by insensitivity of the eigenvalues to changes in the boundary conditions, is usually accompanied by spikiness in the density of states, and sometimes by similar structure in the dynamic susceptibility. For $x=0.5$ we find that the high-frequency excitations are predominantly Ni modes. They are localized even though they exhibit dispersion, which is normally taken to be a sign of delocalization. The energies at which localization is observed can be crudely accounted for by simple arguments based on the relation of the Ising energies to the pure-system spin-wave bands, and on a knowledge of the cluster statistics of the underlying lattice.

(vii) We could find no evidence in $Rb_2Mn_xNi_{1-x}F_4$ for Lifshitz states localized in those statistically rare large regions rich in one spin species. Presumably these states are sufficiently rare that they can not be seen by direct simulation. This implies that split band arguments, while not strictly applicable to this system, are in effect rigorous.

(viii) The numerical and analytic techniques used in this work are generally applicable to any random system. Results for other cases of interest will be presented elsewhere.

ACKNOWLEDGMENTS

We are indebted to Bob Birgeneau and Rich Alben for discussions and for communication of their results before publication. One of us (S. K.) would like to thank Fred Gustavson and Alan Hoffman for instruction on some of the less obvious properties of general matrices, and in numerical matrix methods.

APPENDIX A

A common set of numerical procedures was used in all calculations based upon large Monte Carlo samples of interacting spins. This includes both the static properties of Sec. III and the dynamic properties of Sec. IV, and the densities of states discussed in Sec. II. In this appendix, we describe these procedures, characterize their performance, and contrast them with the molecular dynamics method used in calculation of the dynamic susceptibility by Alben and Thorpe.[11]

Each of the response functions we are concerned with can be written in the form

$$\chi_{\alpha\beta}(\omega)=\langle\alpha|\underline{N}^{-1}(\omega)|\beta\rangle\,, \tag{A1}$$

where $\underline{N}$ was given in Eq. (13). In practice one need not compute $\underline{N}^{-1}$, but can introduce an auxiliary vector, $|\gamma\rangle$, which satisfies[32]

$$\underline{N}|\gamma\rangle = |\beta\rangle . \tag{A2}$$

The desired susceptibility is then

$$\chi_{\alpha\beta} = \langle \alpha|\gamma\rangle . \tag{A3}$$

Linear systems such as (A2) are most economically solved by factorization.[33] Since $\underline{N}$ is symmetric, it can be transformed to the form

$$\underline{N} = \underline{L}\underline{D}\underline{L}^T , \tag{A4}$$

Where $\underline{L}$, a lower triangular matrix, has ones on the diagonal and only zero elements above the diagonal, $\underline{D}$ is a diagonal matrix, and $\underline{L}^T$ is the transpose of $\underline{L}$. Solution of (A2) by back substitution in two stages, using (A4),

$$\underline{L}|\delta\rangle = |\beta\rangle , \tag{A5a}$$

$$\underline{L}^T|\gamma\rangle = \underline{D}^{-1}|\delta\rangle , \tag{A5b}$$

is straightforward, since the triangular form of $\underline{L}$ implies that $\delta_1 = \beta_1$, $\delta_2 = \beta_2 - L_{21}\delta_1$, and so forth.

A second advantage of factorization over direct calculation of $\underline{N}^{-1}$ for our problem is the saving of computer storage space. Essentially all of the elements of $\underline{N}^{-1}$ are nonzero. Thus to calculate $\underline{N}^{-1}$ for an n-by-n sample requires computing and storing $\frac{1}{2}n^4$ quantities. For $n=64$, more than 8×10^6 numbers, an impossible amount, must be stored. On the other hand, the matrix $\underline{L}$ can be kept relatively sparse, and sparse matrix packages exist which, in performing the factorization, will store only the nonzero elements of $\underline{L}$, and carry out only those operations which produce nonzero results. One such package has been described by Gustavson[34] and by Woo *et al.*,[35] and is available commerically.

Factorization into the form (A4) can be viewed as a process of successive elimination of variables from the system of linear equations (A2). The number of fill-ins, or elements of $\underline{L}$ generated depends sensitivity on the order in which the variable are eliminated. A natural strategy is to eliminate spins by rows in the original sample. If the further simplification of free edge rather than periodic boundary conditions is made, all interactions in $\underline{N}$ will be contained within a band of width n about the diagonal. Factorization into the form (A4) then requires $\frac{1}{2}n^4$ operations, and generates $\frac{1}{2}n^3$ nonzero elements of $\underline{L}$. For $n=64$, these are of order 8×10^6 operations, and 1.3×10^5 storage locations. Finally, back substitution requires twice as many operations as there are nonzero elements of $\underline{L}$, or 3×10^5 steps.

It has recently been shown that factorization in $O(n^3)$ steps and generation of $O(n^2\ln_2 n)$ fill-ins is both optimal[36] and feasible.[37] By using George's nested dissection sequence for the five-point difference equation on a planar mesh (described in the appendix of Woo *et al.*[35]), we were able to factor the 64-by-64-site problem, with periodic boundary conditions, in 2×10^6 steps, generating 7×10^4 elements of $\underline{L}$. Generalizations of this optimal ordering also exist to treat the matrices which result from three dimensional problems.

It can be shown that the number of positive eigenfrequencies of (8) less than a given real ω is equal to the number of negative eigenvalues of any matrix $\underline{D}$ which results from a transformation of $\underline{N}(\omega)$ into the form of (A4). Since $\underline{D}$ in this case is diagonal, a count of its negative elements is sufficient to determine the integrated density of states, and from that, $\rho(\omega)$ as discussed in Sec. II.

Typical running times of the programs used, for $n=64$, were 7.5 sec to obtain the integrated density of states at one energy, 10 sec for a static susceptibility, and roughly 1 min to evaluate $\chi''(q, \omega)$, using complex arithmetic, at 14 wave vectors. All programs were run on an IBM 370/168, in an interactive, paged environment.

Alben and Thorpe[11] have recently calculated $\chi''(q, \omega)$ for Monte Carlo samples by integrating forward in time the disturbance resulting from an exciting field $h^*(q)$, using Eqs. (8), and then Fourier transforming the result. The length of time over which they must integrate is inversely proportional to the energy resolution desired. The computing effort associated with the methods used in this paper is independent of resolution, which in our case is determined by the imaginary part added to ω. At the energy resolution of 1.8 meV, typical of the neutron scattering experiments, Alben and Thorpe's procedure appears to be from three to ten times faster than the exact methods. At the energy resolutions which represent the limit of useful data from the finite samples, i.e., from five to ten times the average spacing between eigenvalues, the exact methods appear preferable.

APPENDIX B

In this appendix we give detailed expressions for the effect of a single defect on the response functions. For this purpose the explicit form of the single defect t matrix is introduced. Exact expressions for the magnetic elastic constants K, χ^{ss}, $\chi_\perp$, and A in the limit of low defect concentration are developed. These expressions are valid for bcc, simple cubic, simple square, and centered square antiferromagnets. Simple formulas for the elastic constants at low defect concentration are obtained when the anisotropy energies are much less than the exchange energy. Expressions for the case of nonmagnetic defects are derived from the same treatment, and presented.

The host (A) lattice parameters are denoted by $J_A(=J_{AA})$, S_A, $\hbar\omega_E = 2zJ_AS_A$, g_A, and ω_A. The defect (B) parameters are the spin S_B, the anisot-

ropy frequency, ω_B, g value g_B, and host-defect exchange coupling, $J_B(=J_{AB})$. We also use $\alpha = J_B/J_A$, $\beta = S_B/S_A$, and

$$P_0 = N^{-1} \sum_{\vec{q}} \frac{\omega_E^2}{\omega^2 - \omega(\vec{q})^2} \quad , \tag{B1}$$

$$P_1 = N^{-1} \sum_{\vec{q}} \frac{\omega_E^2 \gamma(\vec{q})^2}{\omega^2 - \omega(\vec{q})^2} \quad . \tag{B2}$$

The p- and d-wave components of the t matrix are given by

$$t_\alpha = V_\alpha (1 - H_\alpha V_\alpha)^{-1} \quad , \quad \alpha \neq s \quad , \tag{B3}$$

where $V_\alpha = \langle \varphi_\alpha | V | \varphi_\alpha \rangle$, and $H_\alpha = \langle \varphi_\alpha | H | \varphi_\alpha \rangle$, and the $|\varphi_\alpha\rangle$ are the symmetry adapted basis functions defined in (32). In the same representation, the s-wave t matrix is

$$t_{11}^{(s)} = \hbar[\omega_E(\alpha - 1) - \Gamma_1(\omega_E + \omega_A - \omega) + \omega_B - \omega_A]/\Delta \quad , \tag{B4a}$$

$$t_{12}^{(s)} = \hbar\omega_E(1 - \alpha + \Gamma_1)/z^{1/2}\Delta \quad , \tag{B4b}$$

$$t_{21}^{(s)} = \hbar\omega_E(\alpha\beta - 1 - \Gamma_1)/z^{1/2}\Delta \quad , \tag{B4c}$$

$$t_{22}^{(s)} = \hbar[\omega_E(1 - \alpha\beta) + \Gamma_0(\omega + \omega_E + \omega_A)]/z\Delta \quad , \tag{B4d}$$

where

$$\Gamma_n = (\omega_A - \omega_B)(1 - \alpha\beta)P_n/\omega_E \tag{B5}$$

and

$$\Delta = \alpha + (\alpha\beta - 1)(\omega - \omega_B)/\omega_E + [(\omega + \omega_A + \omega_E)/\omega_E^2][\omega_A - \omega_B + (\omega_A - \omega)(\alpha - 1) - (\omega_B - \omega)(\alpha\beta - 1)(\omega_E + \omega_A - \omega)/\omega_E]P_0 \quad , \tag{B6}$$

in agreement with Tonegawa.[16]

In the presence of a low concentration of defects we find that

$$\chi(\vec{q}, \omega) = \chi_A(\vec{q}, \omega)(1 + \tfrac{1}{2}c\{\omega_A + \omega_E[1 - \gamma(\vec{q})]\}^{-1} \times \{A_1(\omega)[\omega^2 - \omega(\vec{q})^2] + A_0(\omega) + A_{-1}(\omega)[\omega^2 - \omega(\vec{q})^2]^{-1}\}) \quad , \tag{B7}$$

where

$$\chi_A(\vec{q}, \omega) = \frac{-2g^2\mu_B^2 SN\{\omega_A + \omega_E[1 - \gamma(q)]\}}{\hbar V[\omega^2 - \omega(q)^2]}$$

and $A_n(\omega) = a_n(\omega) + a_n(-\omega)$. We find

$$a_1(\omega) = \eta\delta g(\omega_E + \omega_A)P_0/\omega_E^2 + \eta\delta g\langle \psi_s(\omega) | t^{(s)} | \psi_s(\omega) \rangle/\hbar \quad , \tag{B8a}$$

$$a_0(\omega) = (\eta + \delta g)[\omega_E + \omega_A - \omega_E\gamma(\vec{q})] + \delta g\langle \Omega_s(\omega) | t^{(s)} | \psi_s(\omega) \rangle/\hbar + \eta\langle \psi_s(\omega) | t^{(s)} | \Omega_s(\omega) \rangle/\hbar \quad , \tag{B8b}$$

$$a_{-1}(\omega) = \langle \Omega_s(\omega) | t^{(s)} | \Omega_s(\omega) \rangle/\hbar + \{\omega_A - \omega + \omega_E[1 - \gamma(\vec{q})]\}^2 \times \sum_{\alpha \neq s} |\langle \vec{q} | \varphi_\alpha(\vec{q}) \rangle|^2 \left(\frac{t_\alpha}{\hbar}\right) \quad . \tag{B8c}$$

where $\delta g = g_B/g_A - 1$, $\eta = \beta(1 + \delta g) - 1$, and the components of the vectors appearing in Eqs. (B8) are

$$\langle \Omega_s |_1 = | \Omega_s \rangle_1 = \omega + \omega_A + \omega_E[1 - \gamma(\vec{q})] \quad , \tag{B9a}$$

$$\langle \Omega_s |_2 = - | \Omega_s \rangle_2 = z^{1/2}\gamma(\vec{q})\{\omega_A - \omega + \omega_E[1 - \gamma(\vec{q})]\} \quad , \tag{B9b}$$

$$\langle \psi_s |_1 = | \psi_s \rangle_1 = P_0(\omega + \omega_E + \omega_A)/\omega_E^2 \quad , \tag{B9c}$$

$$\langle \psi_s |_2 = - | \psi_s \rangle_2 = - z^{1/2}P_1/\omega_E \quad . \tag{B9d}$$

The general definition of $\gamma(\vec{q})$ is

$$\gamma(\vec{q}) = \sum_{\vec{\delta}} \frac{e^{i\vec{q}\cdot\vec{\delta}}}{z} \quad .$$

To evaluate $K(c)$ and $A(c)$ we set $g_A = g_B = 1$, $\omega = 0$, and take the limit $\vec{q}^* = \vec{q} - \vec{Q}$ tending to zero, so that, according to Eq. (61),

$$4\mu_B^2 S_{av} \chi^{-1}(\vec{Q} + \vec{q}^*, 0) \sim (2K + Aq^{*2})/S_{av} \quad . \tag{B10}$$

Using Eq. (B7) we find for $\vec{q}^* = 0$,

$$(2/S_{av})K(c) = \hbar\omega_A + c(1, -z^{1/2})t^{(s)}\begin{pmatrix} 1 \\ \sqrt{z} \end{pmatrix} - c(\beta - 1)\delta_A(P_0(1 + \delta_A), -z^{1/2}P_1)t^{(s)}\begin{pmatrix} 1 \\ \sqrt{z} \end{pmatrix} \quad . \tag{B11}$$

Keeping only terms up to order $\delta_A = \omega_A/\omega_E$ and $\delta_B = \omega_B/\omega_E$ we find

$$K^{-1}\frac{dK}{dc} = \frac{K_B - K_A}{K_A} + \beta\frac{(\delta_B - \delta_A)^2}{\delta_A}[(P_0 + 1)\beta - \alpha^{-1}] \quad . \tag{B12}$$

To evaluate $A(c)$ we examine the terms of order q^{*2} in $\chi^{-1}(\vec{Q} + \vec{q}^*, 0)$. Using Eqs. (B7) and (61) we obtain

$$\frac{A(c)}{ba^2S_{av}} = \hbar\omega_E - 2zct^{(p)} - cz^{1/2}(1, -z^{1/2})t^{(s)}\begin{pmatrix} 0 \\ 1 \end{pmatrix} + cz^{1/2}(0, 1)t^{(s)}\begin{pmatrix} 1 \\ \sqrt{z} \end{pmatrix} - c(\beta - 1)(P_0(1 + \delta_A), -z^{1/2}P_1)t^{(s)}\begin{pmatrix} 1 \\ \sqrt{z} \end{pmatrix} + c(\beta - 1)z^{1/2}\delta_A(P_0(1 + \delta_A), -z^{1/2}P_1)t^{(s)}\begin{pmatrix} 0 \\ 1 \end{pmatrix} , \tag{B13}$$

where b depends upon the lattice under consideration through the relation

$$\gamma(\vec{q}) \sim 1 - ba^2q^2 \quad , \tag{B14}$$

as $\vec{q}$ tends to zero. Again, keeping only terms up to order δ_A and δ_B, we find that

$$A^{-1}\frac{dA}{dc} = -2z\frac{t_p}{\hbar\omega_E} - 2(\delta_B - \delta_A)\beta[(\beta - 1)P_0 + (\beta - \alpha^{-1})] \quad . \tag{B15}$$

Finally, to obtain χ^{SS} and $\chi_\perp$ we use (B7) with $\vec{q} = \omega = 0$. Taking $g_A = g_B = 1$, we obtain χ^{SS} to order δ_A and δ_B:

$$(\chi^{ss})^{-1}\frac{d\chi^{ss}}{dc} = -2(\beta-1)^2(P_0+1)+2\beta(1-\alpha)/\alpha-4\delta_A(\beta-\alpha^{-1})(\beta-1)P_0 + \alpha^{-1}(\delta_B-\delta_A)\{(\beta-1)[P_0-(1-\alpha\beta)(1+P_0)]-\tfrac{1}{2}[1+(1-\alpha\beta)(3+4P_0)]\} + [\delta_B(\beta-\alpha^{-1})+P_0(\beta\delta_B-\delta_A)][2\beta/\alpha-2\beta(\beta-1)-1-\beta-2P_0(1-\beta)^2]\,. \quad \text{(B16)}$$

By including the terms involving δg in Eq. (B7), we can calculate $(\chi_\perp)^{-1}\,d\chi_\perp/dc$. Since $\delta g \sim 0.1$ is small, we neglect further corrections of order δ_A or δ_B, and obtain

$$(\chi_\perp)^{-1}\frac{d\chi_\perp}{dc} = (\chi^{ss})^{-1}d\chi^{ss} + 2\beta\delta g\{1-P_0\,\delta g-(2+\delta g)\times[(\beta-1)P_0+\beta-\alpha^{-1}]\}\,. \quad \text{(B17)}$$

The numerical results for low concentrations of Mn in Rb_2NiF_4 are found using $P_0=-2.156$, $\alpha=0.281$, $\omega_B/\omega_E=0.0009$, $\omega_A/\omega_E=0.0084$, $V_p/\hbar\omega_E=\frac{1}{4}(1-\alpha\beta)=0.0746$, and $\hbar\omega_E H_p=1.403$:

$$K^{-1}\frac{dK}{dc}=1.05[(K_{Mn}/K_{Ni})-1]\,, \quad \text{(B18a)}$$

$$A^{-1}\frac{dA}{dc}=-0.827\,, \quad \text{(B18b)}$$

$$(\chi^{ss})^{-1}\frac{d\chi^{ss}}{dc}=18.0\,, \quad \text{(B18c)}$$

$$(\chi_\perp)^{-1}\frac{d\chi_\perp}{dc}=13.4\,. \quad \text{(B18d)}$$

Likewise, for small concentrations of Ni in a Mn host, we use $P_0=-2.361$, $\alpha=3.563$, $\omega_A/\omega_E=0.0046$, $\omega_B/\omega_E=0.0427$, $V_p/\hbar\omega_E=-0.106$, and $\hbar\omega_E H_p=1.423$:

$$K^{-1}\frac{dK}{dc}=0.97[(K_{Ni}/K_{Mn})-1]\,, \quad \text{(B19a)}$$

$$A^{-1}\frac{dA}{dc}=0.691\,, \quad \text{(B19b)}$$

$$(\chi^{ss})^{-1}\frac{d\chi^{ss}}{dc}=0.40\,, \quad \text{(B19c)}$$

$$(\chi_\perp)^{-1}\frac{d\chi_\perp}{dc}=0.22\,. \quad \text{(B19d)}$$

To treat nonmagnetic impurities, we set $\alpha=\beta=0$ and take the limit $\omega_B\to\infty$. The results are

$$A^{-1}\frac{dA}{dc}=-\frac{2zt^{(p)}}{\omega_E}\,, \quad \text{(B20a)}$$

$$K^{-1}\frac{dK}{dc}=-1\,, \quad \text{(B20b)}$$

$$(\chi^{ss})^{-1}\frac{d\chi^{ss}}{dc}=-\frac{4+\delta_A+P_0(1+\delta_A)(\delta_A+2)^2}{(\delta_A+2)[1+\delta_A(1+\delta_A)P_0]}\,. \quad \text{(B20c)}$$

For $\delta_A=0$, these results agree with previous work of Kumar.[38]

APPENDIX C

We wish to evaluate the averaged odd-order moments of $\chi''(\vec{q},\omega)$ and its components $\chi''_{\alpha\beta}(\vec{q},\omega)$ as defined in (18), (20), (86), and (87), where α, β refer to types of atoms. We will present formulas for projected moments $M^n_{\alpha\beta}(\vec{q})$ defined such that

$$\frac{\hbar}{\pi}\int d\omega(\hbar\omega)^n\chi''(\vec{q},\omega)=\sum_{\alpha,\beta}2g_\alpha g_\beta S_\alpha S_\beta M^n_{\alpha\beta}(\vec{q})\mu_B^2\frac{N}{V}\,. \quad \text{(C1)}$$

Two cases have been treated:

$$M^1_{\alpha\beta}(\vec{q})=(g_\alpha g_\beta S_\alpha S_\beta\mu_B^2 N/V)^{-1}\times\langle\vec{q}|\underline{P}_\alpha\underline{\sigma}\underline{W}\underline{\sigma}\underline{P}_\beta|\vec{q}\rangle\,, \quad \text{(C2)}$$

$$M^3_{\alpha\beta}(\vec{q})=(g_\alpha g_\beta S_\alpha S_\beta\mu_B^2 N/V)^{-1}\times\langle\vec{q}|\underline{P}_\alpha\underline{\sigma}\underline{W}\underline{\sigma}\underline{W}\underline{\sigma}\underline{W}\underline{\sigma}\underline{P}_\beta|\vec{q}\rangle\,, \quad \text{(C3)}$$

where $|\vec{q}\rangle$ was defined in (19).

First we separate $\underline{W}$ into its diagonal and off-diagonal parts,

$$W_{ij}=\delta_{ij}d_i+w_{ij}\,, \quad \text{(C4)}$$

where

$$d_i=2\sum_k J_{ik}S_k\,, \quad \text{(C5)}$$

$$w_{ij}=2J_{ij}(S_iS_j)^{1/2}\,, \quad \text{(C6)}$$

and we shall neglect anisotropy terms Δ_i in (C5). $M^1_{\alpha\beta}(\vec{q})$ is readily found to be

$$M^1_{\alpha\beta}(\vec{q})=\delta_{\alpha\beta}2z\langle J_{\alpha\mu}S_\mu\rangle S_\alpha^{-1}-2z\gamma(\vec{q})J_{\alpha\beta}\,, \quad \text{(C7)}$$

where in this appendix $\langle\ \rangle$ will be used to denote a configuration average of the free indices μ or ν (used below) over the types of atoms present.

Evaluation of $M^3_{\alpha\beta}(\vec{q})$ is also straightforward, but lengthy. We first expand the the polynomial $(\underline{\sigma}\underline{W}\underline{\sigma}\underline{W}\underline{\sigma}\underline{W}\underline{\sigma})_{ij}$, collect terms containing 3, 2, 1, or no d's, establish the sign of the product of σ's in each term, and distinguish those cases in which repeated site indexes will affect the configuration average. We obtain

$$(\underline{\sigma}\underline{W}\underline{\sigma}\underline{W}\underline{\sigma}\underline{W}\underline{\sigma})_{ij}=[1]-[2]-[3]-[4]+[5]-[6]+[7]\,, \quad \text{(C8)}$$

where

$$[1]=d_i^3\delta_{ij}\,, \quad \text{(C9a)}$$

$$[2]=w_{ij}(d_i^2-d_id_j+d_j^2)\,, \quad \text{(C9b)}$$

$$[3] = \sum_k w_{ik} w_{kj} (d_i - d_k + d_j)(1 - \delta_{ij}) \,, \tag{C9c}$$

$$[4] = \delta_{ij} \sum_k w_{ik}^2 (2d_i - d_k) \,, \tag{C9d}$$

$$[5] = w_{ij}^3 \,, \tag{C9e}$$

$$[6] = \sum_k w_{ij} [w_{ik}^2 (1 - \delta_{kj}) + w_{jk}^2 (1 - \delta_{ik})] \,, \tag{C9f}$$

$$[7] = \sum_{k,l} w_{ik} w_{kl} w_{lj} (1 - \delta_{kj})(1 - \delta_{il}) \,. \tag{C9g}$$

The contributions of Eqs. (C9) to $M^3_{\alpha\beta}(\vec{q})$ are tabulated below, in a form which is valid for a 3D simple cubic antiferromagnet ($z = 6$), as well as for the 2D square case ($z = 4$). Again we write

$$M^3_{\alpha\beta}(\vec{q}) = [1] - [2] - [3] - [4] + [5] - [6] + [7] \,, \tag{C10}$$

in which

$$[1] = 8z x_\alpha \delta_{\alpha\beta} S_\alpha^{-1} [\langle J^3_{\alpha\mu} S^3_\mu \rangle + 3(z-1)\langle J^2_{\alpha\mu} S^2_\mu \rangle \langle J_{\alpha\mu} S_\mu \rangle + (z-1)(z-2)\langle J_{\alpha\mu} S_\mu \rangle^3] \,, \tag{C11a}$$

$$[2] = 8z\gamma(\vec{q}) x_\alpha x_\beta J_{\alpha\beta} \{ J^2_{\alpha\beta} (S^2_\alpha - S_\alpha S_\beta + S^2_\beta) + (z-1) J_{\alpha\beta} [S_\alpha (2\langle J_{\beta\mu} S_\mu \rangle - \langle J_{\alpha\mu} S_\mu \rangle) + S_\beta (2\langle J_{\alpha\mu} S_\mu \rangle - \langle J_{\beta\mu} S_\mu \rangle)]$$
$$+ (z-1)[\langle J^2_{\alpha\mu} S^2_\mu \rangle + \langle J^2_{\beta\mu} S^2_\mu \rangle - (z-1)\langle J_{\alpha\mu} S_\mu \rangle \langle J_{\beta\mu} S_\mu \rangle + (z-2)(\langle J_{\alpha\mu} S_\mu \rangle^2 + \langle J_{\beta\mu} S_\mu \rangle^2)] \} \,, \tag{C11b}$$

$$[3] = 8z[z\gamma(\vec{q})^2 - 1] x_\alpha x_\beta [\langle J^2_{\alpha\mu} S_\mu (S_\mu - S_\alpha) J_{\beta\mu} \rangle + \langle J_{\alpha\mu} S_\mu (S_\mu - S_\beta) J^2_{\beta\mu} \rangle$$
$$+ (z-1)\langle J_{\alpha\mu} S_\mu J_{\beta\mu} \rangle (\langle J_{\alpha\mu} S_\mu \rangle + \langle J_{\beta\mu} S_\mu \rangle) - (z-2)\langle J_{\alpha\mu} S_\mu J_{\mu\nu} S_\nu J_{\beta\mu} \rangle] \tag{C11c}$$

$$[4] = 8z x_\alpha \delta_{\alpha\beta} [\langle J^3_{\alpha\mu} S_\mu (2S_\mu - S_\alpha) \rangle + 2(z-1)\langle J^2_{\alpha\mu} S_\mu \rangle \langle J_{\alpha\mu} S_\mu \rangle - (z-1)\langle J^2_{\alpha\mu} S_\mu J_{\mu\nu} S_\nu \rangle] \,, \tag{C11d}$$

$$[5] = 8z\gamma(\vec{q}) x_\alpha x_\beta J^3_{\alpha\beta} S_\alpha S_\beta \,, \tag{C11e}$$

$$[6] = 8z(z-1)\gamma(\vec{q}) x_\alpha x_\beta J_{\alpha\beta} (\langle J^2_{\alpha\mu} S_\mu \rangle S_\alpha + \langle J^2_{\beta\mu} S_\mu \rangle S_\beta) \,, \tag{C11f}$$

$$[7] = 8z\gamma(\vec{q})[z^2 \gamma(\vec{q})^2 - 2z + 1] \langle J_{\alpha\mu} S_\mu J_{\mu\nu} S_\nu J_{\nu\beta} \rangle \,, \tag{C11g}$$

and $\gamma(\vec{q})$ is defined in general as

$$\gamma(\vec{q}) = \frac{1}{z} \sum_{\vec{\delta}} e^{i\vec{q}\cdot\vec{\delta}} \,. \tag{C12}$$

APPENDIX D

In this section we evaluate $\mathrm{Im}(\underline{N}^{*-1})$, as required in Eq. (96) to determine the dynamic susceptibility in the four-sublattice approximation. We write $\underline{N}^*$ in block form as four 2×2 submatrices:

$$\underline{N}^* = \begin{pmatrix} D^+ & K \\ K & D^- \end{pmatrix} \,, \tag{D1}$$

where D^σ is a diagonal matrix with elements $(d_{\mathrm{Mn}} + \sigma\omega)$ and $(d_{\mathrm{Ni}} + \sigma\omega)$. The elements of the symmetric matrix K are given by (95). We can factor $\underline{N}^*$ into

$$\underline{N}^* = \begin{pmatrix} 1 & 0 \\ K/D^+ & 1 \end{pmatrix} \begin{pmatrix} D^+ & 0 \\ 0 & D^- - (K/D^+)K \end{pmatrix} \begin{pmatrix} 1 & (1/D^+)K \\ 0 & 1 \end{pmatrix} . \tag{D2}$$

Using the fact that if $\underline{L}$ is a matrix with zeroes everywhere on the diagonal and above, $(\underline{1} - \underline{L})(\underline{1} + \underline{L}) = \underline{1}$, we can write

$$(\underline{N}^*)^{-1} = \begin{pmatrix} 1 & -(1/D^+)K \\ 0 & 1 \end{pmatrix} \begin{pmatrix} (D^+)^{-1} & 0 \\ 0 & [D^- - (K/D^+)K]^{-1} \end{pmatrix} \begin{pmatrix} 1 & 0 \\ -K/D^+ & 1 \end{pmatrix} \,. \tag{D3}$$

If we restrict attention to positive frequencies, $\mathrm{Im}(D^+)^{-1} = 0$, and evaluation of $\chi''(\vec{q}, \omega)$ reduces, upon averaging over the two sublattices, to the 2×2 problem:

$$\chi''(\vec{q}, \omega) = \sum_{\alpha\beta} g_\alpha g_\beta \mu_B^2 (S_\alpha S_\beta x_\alpha x_\beta)^{1/2} \times \mathrm{Im}\{[1 - (1/D^+)K][D^- - (K/D^+)K]^{-1} \times [1 - K/D^+]\}_{\alpha\beta} \,. \tag{D4}$$

We denote the coefficients of $D^- - (K/D^+)K$ as

$$D^- - (K/D^+)K = \begin{pmatrix} C_1 & -C_2 \\ -C_2 & C_3 \end{pmatrix} , \tag{D5}$$

where

$$\begin{aligned} C_1 &= d_A - \omega - a^2(d_A+\omega)^{-1} - b^2(d_B+\omega)^{-1} , \\ C_2 &= ab(d_A+\omega)^{-1} + bc(d_B+\omega)^{-1} , \\ C_3 &= d_B - \omega - b^2(d_A+\omega)^{-1} - c^2(d_B+\omega)^{-1} , \end{aligned} \tag{D6}$$

and a, b, c, the components of the off-diagonal matrix K, are

$$\begin{aligned} a &= 2z\gamma(\vec{q})x_A J_{AA} S_A , \\ b &= 2z\gamma(\vec{q})\, J_{AB}(x_A x_B S_A S_B)^{1/2} , \\ c &= 2z\gamma(\vec{q})\, x_B J_{BB} S_B . \end{aligned} \tag{D7}$$

Using these definitions, the components of $\chi''(\vec{q}, \omega)$ are

$$\begin{aligned} \chi''_{AA} &= x_A g_A^2 \mu_B^2 S_A \operatorname{Im}\Delta^{-1}[C_3 - 2(aC_3 + bC_2)/(d_A+\omega) \\ &\quad + (a^2C_3 + 2abC_2 + b^2C_1)/(d_A+\omega)^2] , \\ \chi''_{AB} &= \chi''_{BA} = g_A g_B \mu_B^2 (x_A x_B S_A S_B)^{1/2} \operatorname{Im}\Delta^{-1}\{C_2 \\ &\quad - (aC_2 + bC_1)/(d_A+\omega) - (bC_3 + cC_2)/(d_B+\omega) \\ &\quad + [abC_3 + (b^2 + ac)C_2 + bcC_1]/(d_A+\omega)(d_B+\omega)\} , \\ \chi''_{BB} &= x_B g_B^2 \mu_B^2 S_B \operatorname{Im}\Delta^{-1}[C_1 - 2(bC_2 + cC_1)/(d_B+\omega) \\ &\quad + (b^2C_3 + 2bcC_2 + c^2C_1)/(d_B+\omega)^2] , \end{aligned} \tag{D8}$$

and when Δ, the determinant of $D^- - (K/D^+)K$ is evaluated at ω_1, a root of the secular equation (97), it gives

$$(2\pi)^{-1} \operatorname{Im}\Delta^{-1} = \frac{(d_A+\omega)(d_B+\omega)\delta(\omega - \omega_1)}{2\omega_1(\omega_1^2 - \omega_2^2)} . \tag{D9}$$

---

*Supported in part by the Office of Naval Research under grant No. N000 14-67-A-0216-0032, and by the National Science Foundation, MRL program, under Grant No. DMR72-03025.

[1]L. de Jongh and A. R. Miedema, Adv. Phys. 23, 1 (1974).
[2]R. A. Cowley and W. J. L. Buyers, Rev. Mod. Phys. 44, 406 (1972).
[3]R. J. Birgeneau, L. R. Walker, R. J. Guggenheim, J. Als-Nielsen, and G. Shirane, J. Phys. C 8, L328 (1975); J. Als-Nielsen, R. J. Birgeneau, H. J. Guggenheim, and G. Shirane, preceding paper, Phys. Rev. B 12, 4963 (1975).
[4]L. T. de Jongh and A. R. Miedema, Adv. Phys. 23, 1 (1974), see Table 6, p. 88.
[5]M. F. Thorpe, Phys. Rev. B 2, 2690 (1970).
[6]H. W. de Wijn, R. E. Walstedt, L. R. Walker, and H. J. Guggenheim, J. Appl. Phys. 42, 1595 (1971).
[7]V. K. S. Shante and S. Kirkpatrick, Adv. Phys. 20, 325 (1971).
[8]J. W. Essam, in *Phase Transitions and Critical Phenomena*, edited by C. Domb and M. S. Green (Academic, New York, 1972), Vol. 2, p. 197.
[9]P. Dean and N. F. Bird, report No. MA 61 of the National Physical Laboratory, Teddington, Middlesex, England (1966) (available from NPL).
[10]E. C. Svensson, W. J. L. Buyers, T. M. Holden, and R. A. Cowley, AIP Conf. Proc. 5, 1315 (1972).
[11]R. Alben and M. F. Thorpe, J. Phys. C 8, L275 (1975).
[12]D. L. Huber, Solid State Commun. 14, 1153 (1974).
[13]B. Velický, S. Kirkpatrick, and H. Ehrenreich, Phys. Rev. 175, 747 (1968).
[14]R. J. Elliott, J. M. Krumhansl, and P. L. Leath, Rev. Mod. Phys. 46, 465 (1974).
[15]T. Tonegawa and J. Kanamori, Phys. Lett. 21, 130 (1966).
[16]T. Tonegawa, Prog. Theor. Phys. 40, 1195 (1968).
[17]S. W. Lovesey, J. Phys. C 1, 102 (1968).
[18]S. Kirkpatrick and A. B. Harris, AIP Conf. Proc. 24, 99 (1974).
[19]R. J. Birgeneau, F. de Rosa, and H. J. Guggenheim, Solid State Commun. 8, 13 (1970).
[20]T. Wolfram and J. Callaway, Phys. Rev. 130, 2207 (1963).
[21]K. Gottfried, *Quantum Mechanics* (Benjamin, New York, 1966), pp. 380ff. Our result for the density of states disagrees with that given in Eq. (5.3) of Ref. 17.
[22]I. M. Lifshitz, Usp. Fiz. Nauk 83, 617 (1964) [Sov. Phys.-Usp. 7, 549 (1965)].
[23]W. K. Holcomb and A. B. Harris, AIP Conf. Proc. 24, 102 (1974).
[24]P. Dean, Rev. Mod. Phys. 44, 127 (1972).
[25]S. Kirkpatrick and T. P. Eggarter, Phys. Rev. B 6, 3598 (1972).
[26]J. T. Edwards and D. J. Thouless, J. Phys. C 5, 807 (1972); D. J. Thouless, Phys. Rep. 13, 93 (1974).
[27]J. Hori and K. Wada, Prog. Theor. Phys. Suppl. 45, 36 (1970).
[28]B. I. Halperin and P. C. Hohenberg, Phys. Rev. 188, 898 (1969).
[29]J. H. Van Vleck, Phys. Rev. 123, 58 (1961).
[30]As mentioned in the Introduction, the Mn anisotropy is of dipolar origin and will therefore be concentration dependent. To take account of this effect, we separate the anisotropy constant K into $K = K_D + K_C$, where K_D is the dipolar contribution and K_C the crystal field contribution. K_D is given by

$$K_D = [x + (1-x)\, g_{Ni} S_{Ni} / g_{Mn} S_{Mn}]^2 K_{Mn}$$

and

$$K_C = (1-x)[K_{Ni} - K_D(1)].$$

This correction can be carried out for $K(x)$ as given by (62) or to the results plotted in Fig. 5. However, the correction leads to a decrease of at most 3% in K, and negligible corrections to other quantities.
[31]A. B. Harris and S. Kirkpatrick (unpublished).
[32]A procedure similar to this was followed in Ref. 20.
[33]G. Forsythe and C. B. Molar, *Computer Solution of Linear Algebraic Systems* (Prentice-Hall, Englewood Cliffs, N. J., 1967).
[34]F. G. Gustavson, in *Sparse Matrices and Their Applications*, edited by D. J. Rose, and R. A. Willoughby (Plenum, New York, 1972), p. 41.
[35]P. T. Woo, S. J. Roberts, and F. G. Gustavson, Society of Petroleum Engineers (AIME) Journal (1974).

[36]A. J. Hoffman, M. S. Martin, and D. J. Rose, SIAM J. Numerical Analysis 10, 364 (1973).
[37]J. A. George, SIAM J. Numerical Analysis 10, 345 (1973); and in *Sparse Matrices and Their Applications*, edited by D. J. Rose and R. A. Willoughby (Plenum, New York, 1972), p. 101.
[38]D. Kumar, Ph. D. thesis (University of Pennsylvania, 1972) (unpublished).
[39]Expressions for A for 3D lattices are given in S. Chikazumi, *Physics of Magnetism* (Wiley, New York, 1964), p. 189. For the pure 2D square lattice, $A = JS^2/c$, where c is the lattice constant perpendicular to the planes of spins.